THE ROLE OF GLIAL CALCIUM CHANGES IN ANIMAL MODELS OF STROKE

Dissertation

zur
Erlangung des Doktorgrades (Dr. rer. nat.)
der
Mathematisch-Naturwissenschaftichen Fakultät
der
Rheinischen Friedrich-Wilhelms-Universität Bonn

vorgelegt von

Dipl.-Biol. CORDULA Marijke RAKERS, geb. Ulbrich

aus
Herdecke

Bonn August 2015

Angefertigt mit Genehmigung der Mathematisch-Naturwissenschaftlichen Fakultät der Rheinischen Friedrich-Wilhelms-Universität Bonn.

1. Gutachter:	Prof. Dr. Gabor Petzold
2. Gutachter:	Prof. Dr. Michael Pankratz

Tag der Promotion: 5. November 2015
Erscheinungsjahr: 2015

Eidesstattliche Erklärung

Ich erkläre hiermit, dass ich diese Dissertation selbstständig ohne Hilfe Dritter und ohne Benutzung anderer als der angegebenen Quellen und Hilfsmittel verfasst habe. Alle den benutzten Quellen wörtlich oder sinngemäß entnommenen Stellen sind als solche einzeln kenntlich gemacht.

Diese Arbeit ist bislang keiner anderen Prüfungsbehörde vorgelegt worden und auch nicht veröffentlicht worden.

Ich bin mir bewusst, dass eine falsche Erklärung rechtliche Folgen haben wird.

Ort, Datum, Unterschrift

Abstract

Ischemic stroke represents one of the leading causes of death and disability. A main characteristic of the early phase of stroke is the spontaneous appearance of peri-infarct depolarizations (PIDs), which are known to negatively affect infarct size and clinical outcome. The aim of this work was to better define the dynamics of PIDs in the peri-infarct region (penumbra), and to investigate the underlying cellular pathways, with a particular emphasis on calcium signaling in astrocytes.

I combined the permanent middle cerebral artery occlusion (pMCAO) stroke model with *in vivo* two-photon (2-P) microscopy in transgenic mice expressing cyan fluorescent protein (CFP) selectively in astrocytes under the Cx43 promoter. Calcium dynamics and local changes in cerebral blood flow (CBF) were measured using the pharmacological calcium indicator Oregon Green 488 BAPTA-1 AM (OGB-1), and blood vessels were visualized by intravenous injection of Texas Red 70 kDa dextran. In addition, astroglial edema – i. e. volume changes in astrocytes during PIDs – was estimated by measuring somatic CFP fluorescence over time. Following pMCAO induction, anesthetized mice were imaged through a cranial window. I found that PIDs could be detected by this technique based on the appearance of a typical propagating wave of calcium changes in neurons and astrocytes that was accompanied by characteristic CBF changes and the development of astrocytic edema. I confirmed the propagation pattern as well as the typical electrophysiological characteristics of PIDs in separate groups by combining pMCAO with extracellular measurements of the direct current (DC) potential and with regional CBF measurements using laser speckle contrast imaging. In addition, the calcium changes in astrocytes during PID were confirmed using a mouse line that expresses the genetically encoded calcium indicator GCaMP3 in astrocytes using a Cre/loxP approach (GLAST-CreERT2:Ai38 line).

Subsequently, I aimed to identify the astroglial signaling pathways underlying calcium transients during PIDs, and their contribution to PID threshold and propagation. To this end, I induced pMCAO in transgenic mouse lines with deletions of inositol triphosphate receptor 2 (IP3R2), transient receptor vanilloid 4 (TRPV4) channel, or aquaporin-4 (AQP4). Each line was crossbred to Cx43-CFP mice for astrocyte identification. In addition, I tested the effect of pharmacological antagonists of these channels in wildtype mice as well as

blockade of the astrocytic sodium calcium exchanger (NCX). I found that the amplitude of astroglial calcium changes during PID was significantly reduced in IP3R2-deficient mice. Calcium transients were also reduced in TRPV4-deficient mice and wildtype mice treated with TRPV4 or NCX blockers. These results indicate that TRPV4 and NCX channels mediate an influx of calcium from the extracellular space, and a substantial calcium release from the endoplasmic reticulum through IP3R2. Surprisingly, no changes were seen in AQP4-deficient mice. Moreover, I found that the delay between pMCAO onset and the first PID, as well as the frequency of subsequent PIDs, was significantly reduced in IP3R2-deficient mice. This was confirmed in separate groups using DC-potential recordings and laser speckle contrast imaging.

In conclusion, I have found that astrocyte-specific IP3R2 is an important contributor to PID threshold, and that IP3R2, TRPV4, and NCX contribute to calcium influx during PID. Since PIDs and cellular calcium overload are important determinants of stroke severity and outcome, pharmacological modulation of these channels in translational or clinical studies may prove therapeutically beneficial.

Contents

1 Introduction 1
1.1 Ischemic Stroke 1
1.1.1 Medical and Socio-Economic Importance 1
1.1.2 Pathophysiology of Ischemic Stroke 2
1.1.3 Peri-Infarct Depolarizations 3
1.2 Astroglia 6
1.2.1 Definition 6
1.2.2 Morphology 7
1.2.3 Physiological Functions of Astrocytes 9
1.2.3.1 Energy Homeostasis 9
1.2.3.2 Network Formation and Synaptic Plasticity 9
1.2.3.3 Cerebral Blood Flow Regulation 10
1.2.4 Communication through Calcium Signals 11
1.2.5 Inositol Triphosphate Receptor 2 (IP3R2) 11
1.2.6 Aquaporin-4 (AQP4) 12
1.2.7 Transient Receptor Vanilloid 4 (TRPV4) Channel 12
1.2.8 Na^+/Ca^{2+} exchanger (NCX) 13
1.3 Astrocytes in Ischemia 13
1.4 Aim of the Study 14

2 Material and Methods 16
2.1 Animals 16
2.2 Groups and Treatment 17
2.3 Techniques 18
2.3.1 Permanent Middle Cerebral Artery Occlusion (pMCAO) 18
2.3.2 Cranial Window Preparation 20
2.3.3 Two-Photon Microscopy 21
2.3.4 Laser Speckle Contrast Imaging 23
2.3.5 Electrophysiology 23
2.3.6 Immunofluorescence 24
2.3.7 Cre/loxP System 24

2.3.8 Genotyping 25
2.3.9 Buffers and Solutions 26
2.4 Data Analysis and Statistics 27
2.4.1 Two-Photon Data Analysis 27
2.4.2 Laser Speckle Contrast Data Analysis 29
2.4.3 Analysis of Electrophysiological Data Analysis 29
2.4.4 Statistics 30

3 Results 31
3.1 Identification of the Penumbra with Laser Speckle Contrast Imaging 31
3.2 Electrophysiological Measurements of PIDs 34
3.2.1 IP3R2 Deletion Reduces PID Occurrence and Increases Latency to First PID 36
3.3 Two-Photon Microscopy 39
3.3.1 Alexa Fluor 633 Labels Penetrating Arterioles 39
3.3.2 Simultaneous Imaging of CBF, Calcium, and Edema during pMCAO 40
3.3.3 Cerebral Blood Flow Measurement during pMCAO 42
3.3.4 Imaging of Calcium Transients during the First Detected PID 44
3.3.4.1 IP3R2 Deletion and Trpv4 Deletion Attenuated Calcium Signals during PIDs 46
3.3.4.2 Identification of DMSO as a Suitable Diluent for Calcium Imaging Experiments Using Pharmacological Inhibitors 48
3.3.4.3 TRPV4 Blockade Attenuated Calcium Signals in Astrocytes and Neurons, and NCX Blockade Slowed Neuronal Calcium Signals 50
3.3.4.4 Velocity of Calcium Waves within Astrocytes, Neurons, and Neuropil during PIDs 52
3.3.5 Edema Measurement 53
3.4 Systemic Physiological Monitoring 54
3.5 Investigating PIDs Using a Genetic Calcium Indicator Approach – Preliminary Data 55
3.5.1 Quantification 55
3.5.2 Two-Photon Imaging of GLAST-CreERT2:Ai38 Mice 57

4 Discussion 59
4.1 *In vivo* Imaging of Early PIDs in the Cortical Penumbra after pMCAO 59
4.2 The Role of Glial Calcium Transients during PIDs 61
4.2.1 Calcium Transients during PIDs are Mediated by IP3R2, TRPV4, and NCX 61
4.2.2 IP3R2 Mediate the Threshold for PIDs 62
4.2.3 AQP4 is not Involved in PID-related Calcium Signaling or Edema Formation 63
4.2.4 CBF Changes during PIDs 63
4.3 Pathophysiological Relevance 64

5 Appendix 65
5.1 List of Figures 67
5.2 List of Tables 68
5.3 Abbreviations 69
6 List of Publications 70
7 Acknowledgement 71
8 Bibliography 73

1 Introduction

1.1 Ischemic Stroke

1.1.1 Medical and Socio-Economic Importance

Despite many years of basic, translational, and clinical brain research, stroke still represents one of the leading causes of death and disability. In Germany, 262,000 new or recurrent strokes were diagnosed and 63,000 people died from the disease in 2008 (Heuschmann et al., 2010). This equates to one stroke every 2 minutes and one death from stroke every 8 minutes. Most survivors suffer from long-term disabilities. For example, the total costs per first-year survivor of first-ever ischemic stroke in 2004 amounted to € 7.1 billion, including treatment (62 %), rehabilitation (21 %), and nursing (17 %) (Kolominsky-Rabas et al., 2006).

The origin of a stroke can be *ischemic* (clot) or *hemorrhagic* (bleeding). 87 % of all strokes are ischemic: An embolus or thrombus occludes a cerebral blood vessel and prevents blood supply to a certain part of the brain, causing necrotic and apoptotic neuronal cell death in the tissue distal to the occluded vessel (Go et al., 2014) (Figure 1-1). Risk factors for stroke can be unmodifiable (e.g. gender, age, and race) or modifiable by medication or change of social behavior or lifestyle (e.g. high blood pressure, atrial fibrillation, high cholesterol, diabetes, atherosclerosis as well as smoking, excessive alcohol consumption, and sedentary lifestyle) (Hankey, 2006).

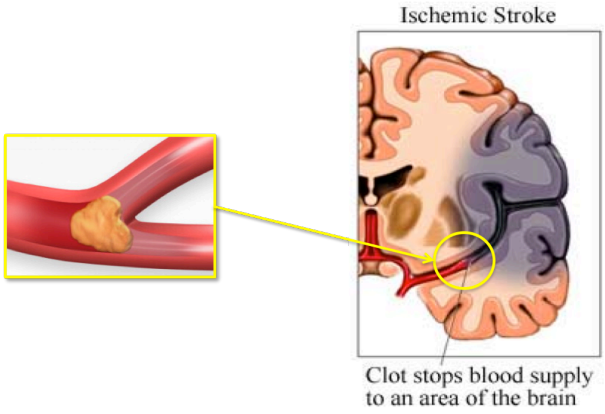

Figure 1-1: Ischemic stroke. Bifurcation occluded by an embolus. Blood supply to a brain artery is blocked (e.g. middle cerebral artery), causing loss of oxygen and glucose in certain brain parts. Cells will die from necrosis after energy deprivation in the acute phase as well as from neuroinflammation in later stages. (Adapted from www.strokeassociation.org and www.edocamerica.com.)

1.1.2 Pathophysiology of Ischemic Stroke

The brain depends on the steady supply of blood containing oxygen and glucose given the large energy demands of neuronal activity and the fact that the brain possesses minimal energy stores. During ischemia, *cerebral blood flow* (CBF) is locally reduced, leading to a depletion of oxygen and glucose in that brain region. The consequence is primary or secondary neuronal death in tissue supplied by the affected arteries.

After stroke onset, ischemic tissue can be divided into an *infarct core* and a *penumbra*. In the core, cells start to die instantly after occlusion, whereas in the penumbra (i.e. the tissue surrounding the core) cells are metabolically stressed but have the potential to recover (Hossmann, 1996). However, unless the penumbra is rescued early during stroke development by restoration of CBF to normal levels or other neuroprotective interventions, neurons are either recruited to the necrotic infarct core and suffer from acute cell death (primary neuronal cell death) or die later from apoptosis (secondary neuronal cell death). Therefore, the penumbra is a damaged but potentially salvageable ischemic region, and thus, a better understanding of the mechanisms leading to cell death in the penumbra could have important consequences for stroke outcome.

Spontaneously occurring *peri-infarct depolarizations* (PIDs) are one of the main pathophysiological features of the penumbra and a leading cause of neuronal death in penumbral tissue after ischemia.

1.1.3 Peri-Infarct Depolarizations

As mentioned above, the infarct is divided into a core and a penumbra. The core develops where CBF during artery occlusion is lowest (about <20 % of baseline) (Hossmann, 1994a). In this area, neurons instantly die from energy failure, resulting in loss of membrane potentials and breakdown of ion homeostasis in the surrounding tissue. An overload of extracellular glutamate and potassium leads to the spontaneous development of an *anoxic depolarization* (AD) (Moskowitz et al., 2010). This is an electrochemical wave of spreading depolarization travelling from cell to cell at 2-5 mm/min (Hartings et al., 2003). The depolarization is accompanied by a negative shift of the direct current (DC) potential. In the ischemic core, this depolarization is terminal, i.e. neurons cannot repolarize due to the lack of oxygen and glucose (Dreier, 2011).

At the rim of the ischemic core, the anoxic depolarization wave travels into the penumbra, where CBF has remained at 20-40 % of CBF baseline level, i.e. a level that is sufficiently high for repolarization (Hossmann, 1994a). Hence, these depolarization waves in the penumbra – known as peri-infarct depolarizations (PIDs) – are transient and not terminal, but the metabolic burden imposed on penumbral tissue during each depolarization and subsequent repolarization is extremely high. In addition, CBF is already reduced in the penumbra, and cannot compensate adequately to match the increased metabolic demand – in fact, each depolarizing wave is accompanied by progressive CBF reduction (Figure 1-2) (Shin et al., 2006) instead of the physiological CBF increase termed *functional hyperemia* (Dreier, 2011; Petzold and Murthy, 2011). In addition, spreading depolarizations induce an influx of calcium into neurons and astrocytes, thereby amplifying cell death induced by calcium overload (Nicotera et al., 1992).

Further away from the stroke, PIDs continue to propagate into healthy brain areas as relatively innocuous *cortical spreading depression* (CSD), which is accompanied by a physiological CBF increase (Petzold et al., 2005; Dreier, 2011).

In summary, each PID wave leads to an amplification of neuronal death and subsequent expansion of the infarct core at the expense of the penumbra. This is also exemplified by the fact that the occurrence and cumulative duration of PIDs are correlated with infarct size (Mies et al., 1993; Dijkhuizen et al., 1999). The temporal correlation between PIDs and cell death is demonstrated in Figure 1-3 (Dirnagl et al., 1999).

One cell type that plays a central, yet understudied, role in spreading depolarization waves are astrocytes. I will therefore summarize in the next chapter the role of astroglia in normal brain function and ischemia.

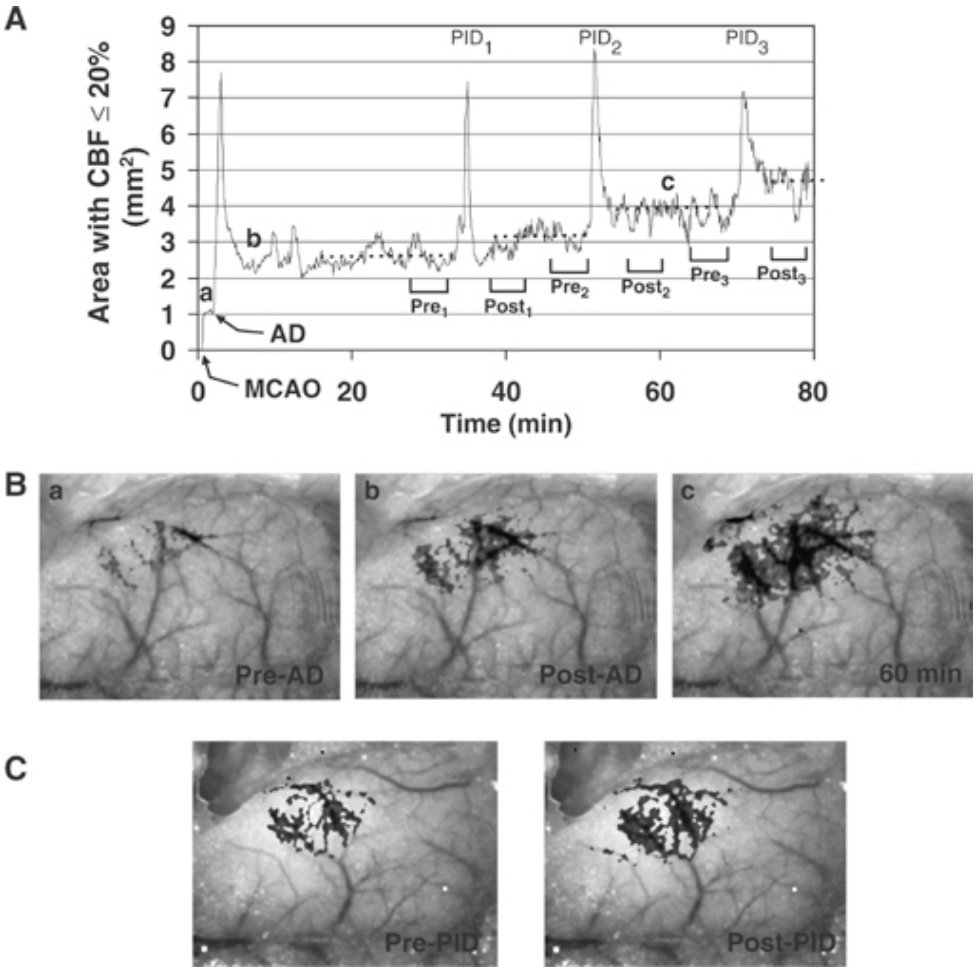

Figure 1-2: Expansion of severely hypoperfused cortex during AD and PIDs in acute focal ischemia (MCAO). A) ADs and PIDs are temporally related to acute expansion of hypoperfused territory. B) Speckle contrast images show the expansion of severely hypoperfused territories (i.e. ≤ 20 % residual CBF) within 60 min (in black). (Reprinted by permission from Macmillan Publishers, from Shin et al., 2006.)

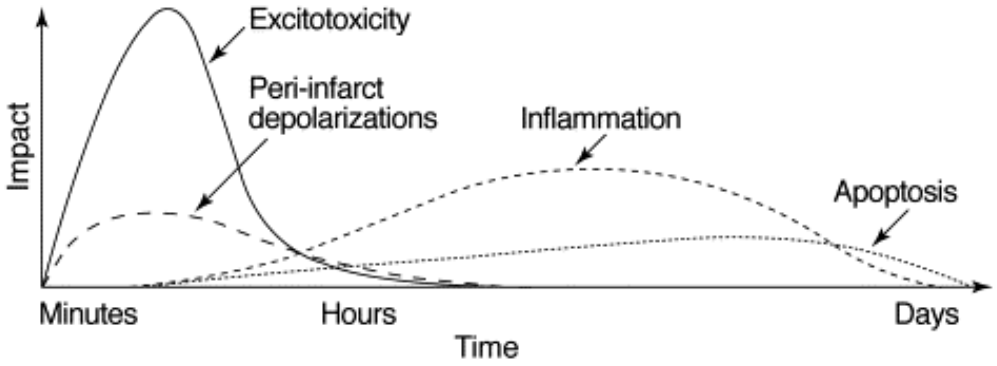

Figure 1-3: Putative cascade of damaging events in focal cerebral ischemia. Very early after the onset of the focal perfusion deficit, excitotoxic mechanisms can damage neurons and glia lethally. In addition, excitotoxicity triggers a number of events that can further contribute to the demise of the tissue. Such events include peri-infarct depolarizations and the more-delayed mechanisms of inflammation and programmed cell death. The x-axis reflects the evolution of the cascade over time, while the y-axis aims to illustrate the impact of each element of the cascade on final outcome. (Reprinted from Science Direct, Dirnagl et al., 1999.)

1.2 Astroglia

1.2.1 Definition

Besides neurons, the mammalian brain consists to a great extent of glia (= *glue*) cells. The most numerous and diverse type of the latter are astrocytes, also termed *astroglia*. They have first been described by Mihály Lenhossék in the 19th century as "astrocytes" based on their star-like shape (*astron* = star; *kytos* = cell) (Lenhossék, 1891; Verkhratsky et al., 2012; Kettenmann and Verkhratsky, 2013). Two main types of astrocytes are differentiated: *Protoplasmic* and *fibrous* astrocytes. Protoplasmic astrocytes are located in the gray matter and have large processes, while fibrous astrocytes are found in white matter and have little to moderate branching. Like other glial cells, astrocytes were traditionally regarded as "passive" cells, due to the fact that they are physiologically non-excitable, i.e. they do not produce action potentials like neurons. However, they express different ion channels and neurotransmitter receptors, which enable them to respond to external signals with intracellular calcium transients (Verkhratsky and Steinhauser, 2000; Verkhratsky, 2006). Since the late 1980s, increasing evidence

has shown that astrocytes are regulators of the neurovascular unit and strongly influence cellular development and inflammation processes (Volterra and Meldolesi, 2005).

1.2.2 Morphology

It is now accepted that not all astrocytes are uniformly star-shaped, but that they are extremely heterogeneous cells. Every astrocyte has a different morphology and varies in the number and length of branches. Additionally, they do not only differ in morphology but also in location, physiology and function (Emsley and Macklis, 2006). My focus here is on the highly differentiated protoplasmic astrocytes localized in the cortex of the brain that are strongly affected by ischemic stroke. In contrast to fibrous astrocytes, the branches of protoplasmic astrocytes can contact other astrocytes with thousands of processes and *endfeet*. Protoplasmic astrocytes are coupled with each other by *gap junctions* and form large astrocytic networks called *syncytia* (Figure 1-4). However, astrocytes do not only contact other astrocytes but also neurons and blood vessels where they are able interact with other cells of the neurovascular unit (Petzold and Murthy, 2011). The dynamic concept in synaptic physiology, where an astrocyte contacts pre- and postsynaptic neuronal terminals, is called the *tripartite synapse*. Bidirectional communication between neurons and astrocytes within the tripartite synapse is reflected by the transmission of neuro- and gliotransmitters through the synaptic cleft.

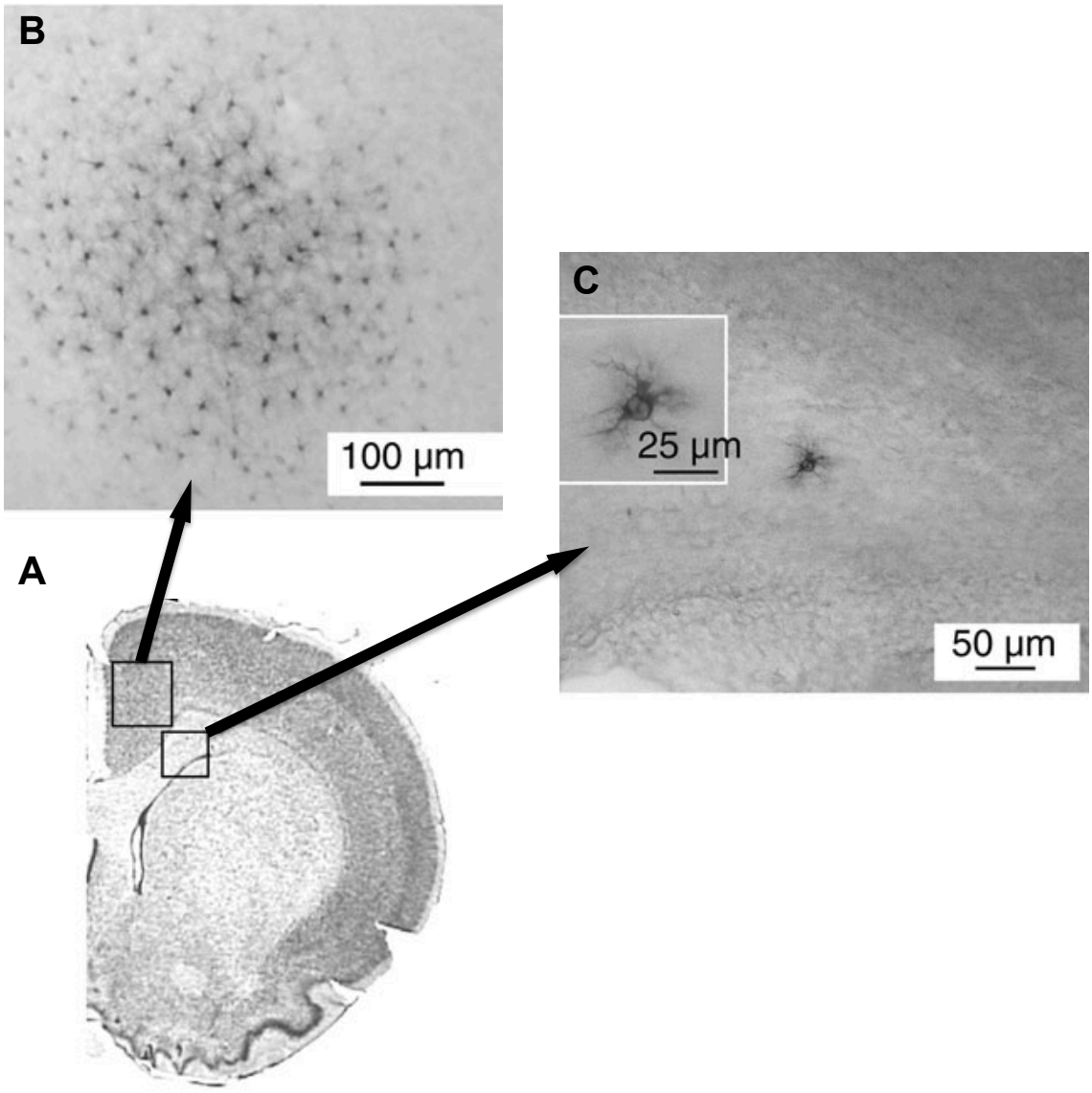

Figure 1-4: Astrocytic coupling in the neocortex compared to the corpus callosum. A) Biocytin was injected into one protoplasmic astrocyte of the neocortex and one fibrous astrocyte in the corpus callosum from a GFAP/EGFP transgenic mouse. Astrocytes were selected using their fluorescence at 488 nm. A 150-µm-thick slice was used for demonstration of the injection sites. B) Injection into a protoplasmic astrocyte labels a large population of astrocytes (*syncytium*) on a 50-µm-thick slice. C) In the corpus callosum, only a single cell is stained with biocytin on a 150-µm-thick slice. The insert is a magnified image of the single injected cell. (Adapted from Haas et al., 2006, by permission of Oxford University Press.)

1.2.3 Physiological Functions of Astrocytes

1.2.3.1 Energy Homeostasis

The primary responsibility of astrocytes is to control the homeostasis of the nervous system (Petzold and Murthy, 2011; Verkhratsky et al., 2012). Under physiological conditions, astrocytic glycogen stores provide metabolic help for neurons in form of glucose and lactate (Giaume et al., 2010), i.e. neurons depend on energy supply from astrocytes. Furthermore, astrocytes act as a *potassium buffer* (Kofuji and Newman, 2004) and thereby help to shape neuronal depolarization kinetics. Another important feature of astrocytes is the protection of neurons from *reactive oxygen species* (ROSs) (Desagher et al., 1996).

1.2.3.2 Network Formation and Synaptic Plasticity

Astrocytes contact neurons and can modulate neuronal function by the release of *gliotransmitters* (e.g. glutamate, D-serine, and ATP) (Giaume et al., 2010). Astrocytic endfeet cover most neuronal synapses and modulate the integration of synaptic information (Haydon, 2001). In contrast to neurons, astrocytes are not electrically excitable. Instead of creating actions potentials, they react to external signals with internal calcium transients. Within the tripartite synapse, they modulate synaptic input on the postsynaptic site by the subsequent release of gliotransmitters, as shown in Figure 1-5. Thereby, astrocytes do not only facilitate transient synaptic strength but also play a role in long-term potentiation (Henneberger et al., 2010).

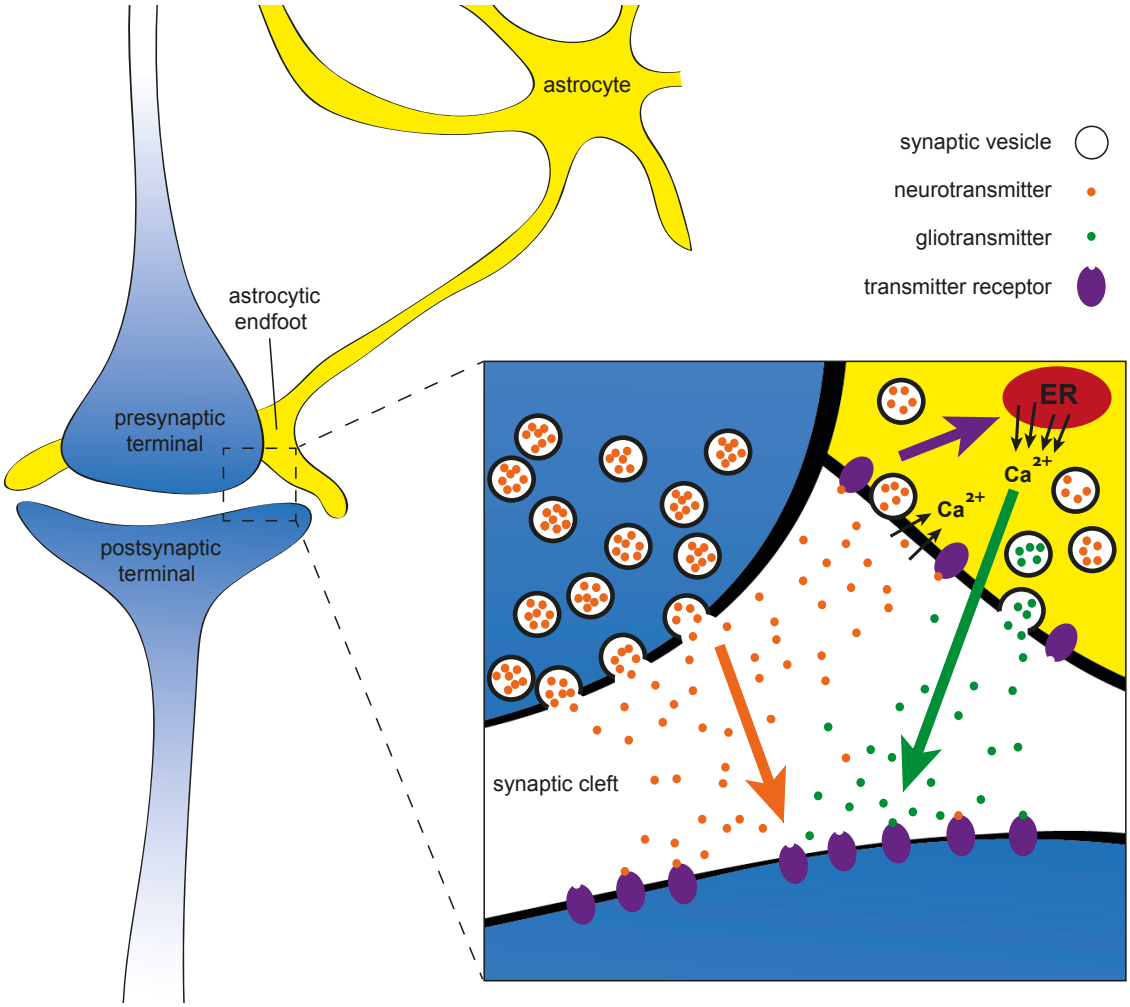

Figure 1-5: Modulation of synaptic input within the tripartite synapse. A neuron releases neurotransmitters into the synaptic cleft, which an astrocyte contacts with one of its endfeet. Neurotransmitters trigger calcium transients in astrocytes from the extracellular space or internal stores, such as the endoplasmic reticulum (ER), into the cytosol. Subsequently, astrocytes react with the release of gliotransmitters and thereby modulate the communication between the pre- and postsynaptic site.

1.2.3.3 Cerebral Blood Flow Regulation

In the brain, neuronal activation is closely coupled to CBF responses. Already in the 19th century, Roy and Sherrington described local variations of blood supply in response to neuronal activity (Roy and Sherrington, 1890). This phenomenon is termed *functional hyperemia* or *neurovascular coupling*. It plays an important role in current research as it strongly influences brain pathology in many diseases. In 1903, Golgi described that astrocytes embrace brain capillaries and he presumed a metabolic connection between neurons and blood vessels (Golgi, 1903). In fact, astrocytic endfeet are located around cerebral blood vessels and are able to

regulate CBF by the release of vasoactive factors (Verkhratsky, 2006). After neuronal activity, increases of calcium in astrocytic endfeet do not only lead to the release of gliotransmitters but also to the release of vasoactive substances triggering either *vasoconstriction* or *vasodilatation* (Iadecola and Nedergaard, 2007; Attwell et al., 2010; Petzold and Murthy, 2011).

1.2.4 Communication through Calcium Signals

As mentioned above, astrocytes do not create all-or-none-reactions in the form of action potentials, but their way of signaling is the creation of dynamic calcium transients. Astroglial calcium can act as a 2nd messenger in several signal pathways that contribute to, e.g., CBF regulation, inflammatory processes, or synaptic strength (Verkhratsky et al., 2012). Astrocytes have two different possibilities to generate a calcium signal: the cell either releases calcium from internal stores, mainly over the IP3 (inositol triphosphate) pathway, or calcium enters the cell from the extracellular space through different channels located in the plasma membrane. In this study, some potentially relevant proteins are investigated regarding their function in calcium transients during PIDs. IP3 receptor 2 (IP3R2) for internal calcium release, and three membrane channels/transporters that potentially carry calcium from the extracellular space into the cell: Aquaporin-4 (AQP4), transient receptor vanilloid 4 (TRPV4) channel, and the Na^+/Ca^{2+} exchanger (NCX). In the following, these proteins will be explained in more detail.

1.2.5 Inositol Triphosphate Receptor 2 (IP3R2)

In astrocytes, the endoplasmic reticulum (ER) is the cell compartment that is most capable of internal calcium storage. IP3R2 is directly attached to the ER of astrocytes and is responsible for internal calcium release after activation of the IP3 pathway (Petravicz et al., 2008). External signals trigger IP3R2 activity via Gq-G-protein coupled receptors (GqPCRs), such as metabotropic glutamate receptors. The GqPCR activates Phospholipase C (PLC) that subsequently hydrolyzes phosphatidylinositol 4,5-bisphosphate (PIP2) to IP3 and diacylglycerol (DAG). IP3 can then bind to IP3R2 that finally leads to calcium release from the

ER, resulting in a strong and sustained increase of the cytosolic calcium concentration. Calcium from internal stores appears to be singularly released by the IP3R subtype IP3R2: While neurons showed unchanged calcium reactions in IP3R2-kos, somatic calcium signals in astrocytes were completely blocked (Petravicz et al., 2008). More recent studies have confirmed a strong reduction of spontaneous calcium events in IP3R2-ko astrocytes, but have also shown that some calcium transients, most likely mediated through membrane-anchored channels, are still detectable (Haustein et al., 2014; Srinivasan et al., 2015).

1.2.6 Aquaporin-4 (AQP4)

AQP4 is a channel protein for water transport. It is abundantly expressed in astrocytic endfeet at the blood-brain barrier (BBB) (Zador et al., 2009), where it can increase the water permeability of the cell membrane up to 50-fold (Day et al., 2014). The two isoforms AQP4-M1 and AQP4-M23 are arranged in *orthogonal array particles* (OAPs) within the cell membrane. Water influx through AQP4 can create cellular edema (Badaut et al., 2011) or even initiate calcium spikes, either due to calcium permeability of AQP4 or by AQP4 being physically coupled to other calcium-permeable channels (Benfenati et al., 2011) gated by other mechanisms, such as stretch-activated channels (Thrane et al., 2011).

1.2.7 Transient Receptor Vanilloid 4 (TRPV4) Channel

The TRPV4 channel is a non-selective cation channel and therefore also permeable for calcium. It can be activated by different stimuli, including heat, different chemical compounds, and cell swelling (Vriens et al., 2004). In cortical astrocytes, TRPV4 was not only confirmed to be localized in the plasma membrane but also, like AQP4, seems to be involved in calcium increases within edema formation (Benfenati et al., 2007). Later, it was hypothesized that TRPV4 and AQP4 might be physically linked (Benfenati et al., 2011). An *in vivo* study on Trpv4-ko mice suggested that TRPV4-gated calcium transients in astrocytic endfeet can lead to subsequent calcium release from internal stores through IP3R2 activation, and might also contribute to neurovascular coupling (Dunn et al., 2013).

1.2.8 Na^+/Ca^{2+} exchanger (NCX)

NCX is responsible for the bi-directional membrane transport of sodium and calcium, exchanging 3 Na^+ for 1 Ca^{2+} (Jeffs et al., 2007). The transfer direction depends on the sodium gradient that is driving the antiport. Under physiological conditions, the transporter functions in "forward" mode: The inward force of sodium, which predominates the extracellular space, drives the outward transport of calcium. Under pathophysiological conditions, such as ischemia, NCX can function in "reverse" mode due to intracellular sodium overload, resulting in an extrusion of sodium on the expense of calcium transport into astrocytes (Parpura and Verkhratsky, 2012). Therefore, "reverse" mode NCX has been proposed as an important contributor to astroglial calcium changes under ischemic conditions (Annunziato et al., 2004).

1.3 Astrocytes in Ischemia

Ischemia causes a mismatch between blood supply and energy (glucose) consumption. High ionic imbalance in the extracellular space disturbs the supportive dynamics between astrocytes and neurons. The breakdown of ionic and energy homeostasis represents one of the main challenges for the nervous system in ischemic stroke.

An increase in the calcium concentration in astrocytes strongly impacts astrocytic function during ischemia and may even influence the infarct size: Ding et al., (2009) showed that calcium-dependent glutamate release from astrocytes during calcium waves contributes to neuronal damage in a photothrombotic model of ischemia. Moreover, neurovascular coupling is attenuated in cerebral ischemia (Petzold and Murthy, 2011) and elevated calcium concentrations in astrocytes may also directly induce vasoconstriction (Mulligan and MacVicar, 2004). Both may contribute to the inadequate response of CBF during ADs and PIDs (Shin et al., 2006; Chuquet et al., 2007) and indicate that astroglial (dys-) regulation of CBF may contribute to neuronal injury after stroke.

Besides possible consequences of astroglial calcium changes for CBF regulation in ischemia, other points to consider are the implications of calcium influx into

astrocytes for neuronal calcium overload as well as for the generation and propagation of PIDs. During neuronal depolarizations, such as in the early phase of ischemia or during PIDs, glutamate is released synaptically and activates the astroglial IP3 signal pathway via metabotropic glutamate receptors on astrocytes. Subsequently, large astrocytic calcium transients are generated by activation of IP3R2 in the ER (Petravicz et al., 2008). This astroglial IP3R2-mediated calcium increase may in turn lead to the release of gliotransmitters from astrocytes, such as glutamate and ATP (Nedergaard et al., 2010), possibly inducing a vicious circle in which neuronally derived glutamate triggers more glutamate release from astrocytes, which in turn will further amplify calcium overload and excitotoxicity in neurons, and may also modulate the threshold for PIDs. Yet, the role of IP3R2 in these mechanisms has so far remained largely unexplored.

Similarly, the astrocytic membrane-anchored channels/transporters studied here – AQP4, TRPV4, and NCX – may also have important consequences for PID threshold and propagation as well as neuronal survival. First, calcium entry into astrocytes through all of these channels may play a similar role in ischemia as IP3R2 described above. Second, AQP4 contributes to cellular edema and increased stroke volume (Manley et al., 2000), whereupon swelling in the perivascular astrocytic endfeet during PIDs might mechanically compress blood vessels and thereby further reduce local CBF. Third, TRPV4 mRNA and protein are up-regulated after ischemia (Butenko et al., 2012), and TRPV4 is activated by mechanisms occurring during ischemia such as cellular edema, suggesting an involvement in the early phase of ischemia and maybe even in PIDs. Fourth, a reverse-mode action of NCX (described above) (Annunziato et al., 2004) may affect PID threshold not only through the accumulation of calcium in astrocytes, but also by extracellular extrusion of sodium, which may then further depolarize neurons.

1.4 Aim of the Study

The aim of current stroke research is to rescue the penumbra from cell death. Treatment options are limited and all restricted to the first few hours after stroke onset. It is therefore necessary to find alternate treatment solutions, which can

ameliorate stroke outcome particularly in the later stages of stroke and directly act on the penumbra. One very attractive target that fulfills all of these criteria are PIDs. However, the cellular pathways underlying PIDs have remained largely unknown. Therefore, the aim of this work was to investigate the role of important routes leading to calcium elevations in astrocytes – IP3R2, AQP4, TRPV4, and NCX – for PID development and propagation. Moreover, I aimed to investigate the effect of these astroglial calcium transients on CBF changes during PIDs as well as astrocytic edema.

2 Material and Methods

2.1 Animals

C57BL/6N or CD1 male mice (3-5 months) underwent routine cage maintenance once a week and microbiological monitoring according to the Federation of European Laboratory Animal Science Associations recommendations. Mice were housed on a 12-h light/dark cycle with food (Sniff Spezialdiäten, Germany) and water available *ad libitum*. Research and animal care procedures were approved by the Review Board for the Care of Animal Subjects of the district government (North Rhine-Westphalia, Germany) and performed according to international guidelines on the use of laboratory animals.

Origins of the transgenic animals and their references are listed in Table 1. Cx43-CFP$^{+/-}$ mice with fluorescent astrocytes were crossbred to C57Bl/6N wildtypes and different knockout lines: 1) IP3R2-ko, 2) Trpv4-ko, and 3) Aqp4-ko. Because of the different genetic background of the Aqp4-knockouts, a separate control group was included comparing knockouts from the F1 generation to their wildtype littermates. Cx43-CFP$^{+/-}$ genotype was used for 2-P imaging and Cx43-CFP$^{-/-}$ for electrophysiology or laser speckle contrast imaging. Cx43-CFP$^{+/-}$/Trpv4$^{-/-}$ and Cx43-CFP$^{+/-}$/IP3R2$^{-/-}$ mice bred slowly so I used Cx43-CFP$^{-/-}$ mice for some 2-P microscopy experiments. For the identification of astrocytes in these mice, astrocytes were labeled with Sulforhodamine 101 (SR101) (Nimmerjahn et al., 2004). Cx43-CreERT2 and GLAST-CreERT2 lines were crossbred to the Ai38 mouse line from the Jackson Lab (JAX stock no. 014538) for GCaMP3 imaging.

Table 1: List of transgenic animals.

mouse line	background	generated by	reference	provided by
Cx43-CFP	C57Bl/6N	Prof. Martin Theis (University of Bonn)	Longa et al., 1989; Degen et al., 2012	Prof. Martin Theis (University of Bonn)
IP3R2-ko	C57Bl/6N	Prof. Ju Chen (UC San Diego)	Li et al., 2005; DongThe Allen Institute for Brain Science, 2008	Prof. Andrea Volterra (University of Lausanne)
TRPV4-ko	C57Bl/6N	Prof. Wolfgang Liedtke (Duke University)	Liedtke and Friedman, 2003	Prof. Wolfgang Kübler (Charité, Berlin)
Aqp4-ko	CD1	Prof. Alan Verkman (UCSF)	Manley et al., 2000	Prof. Christian Steinhäuser (University of Bonn)
Cx43-CreERT2	C57Bl/6N	Prof. Martin Theis (University of Bonn)	Eckardt et al., 2004; Schindelin et al., 2012	Prof. Martin Theis (University of Bonn)
GLAST-CreERT2	C57Bl/6N	Prof. Jeremy Nathans (Johns Hopkins University)	Kang et al., 2010b	JAX Labs (Stock No. 012586)
Ai38	C57Bl/6N	Hongkui Zeng (Allan Institute for Brain Science)	Zariwala et al., 2012	JAX Labs (Stock No. 014538)

2.2 Groups and Treatment

Group 1 (Cx43-CFP$^{+/-}$ for 2-P imaging or Cx43-CFP$^{-/-}$ for electrophysiology) represented a control group for IP3R2-kos and Trpv4-kos (IP3R2/Trpv4-ctrl). Group 2 (Cx43-CFP$^{+/-}$/IP3R2$^{-/-}$ and Cx43-CFP$^{-/-}$/IP3R2$^{-/-}$ for 2-P imaging; Cx43-CFP$^{-/-}$/IP3R2$^{-/-}$ for electrophysiology) are IP3R2-knockouts. Group 3 (Cx43-CFP$^{-/-}$/Trpv4$^{-/-}$ for 2-P imaging and electrophysiology) are Trpv4-knockouts. Group 4 (Cx43-CFP$^{+/-}$/Aqp4$^{+/+}$ for 2-P imaging; Cx43-CFP$^{-/-}$/Aqp4$^{+/+}$ for electrophysiology) represents the separate control group for Aqp4-knockouts. Group 5 (Cx43-CFP$^{+/-}$/Aqp4$^{-/-}$ for 2-P imaging; Cx43-CFP$^{-/-}$/Aqp4$^{-/-}$ for electrophysiology) are the according Aqp4-knockouts. Group 6 and 7 are different diluents tested before dilution of blockers (group 6: 0.1 % dimethyl sulfoxide (DMSO, 99.9 %, Sigma) in PBS, group 7: 10 % Cremophor EL (Sigma) in PBS). Group 8 included the TRPV4-blocker HC-067047, group 9 the AQP4-blocker AqB013 (both 100 µM, diluted in 0.1 % DMSO), and

group 10 the NCX blocker KB-R7943 (500 µM, diluted in 0.1 % DMSO). I topically applied the different blocker solutions on the cortex before MCAO induction for 45 min.

In two separate groups, 11 (Cx43-CreERT2$^{+/-}$/Ai38$^{fl/-}$) and 12 (GLAST-CreERT2$^{+/-}$/Ai38$^{fl/fl}$, GLAST-CreERT2$^{+/-}$/Ai38$^{fl/-}$), animals were injected IP with tamoxifen (100 mg in 5 ml/kg bw for five days, diluted in 1:10 EtOH in sunflower oil). GLAST-CreERT2:Ai38 mice were injected at the age of 3 weeks and Cx43-CreERT2:Ai38 mice 3 weeks before surgery.

2.3 Techniques

2.3.1 Permanent Middle Cerebral Artery Occlusion (pMCAO)

The mouse was placed on its back and an incision was made above the thyroid gland. The left CCA (common carotid artery) was separated from the surrounding tissue and the vagus nerve. Then it was ligated with a suture (Suprama, Germany) 3-4 mm proximal to the bifurcation, which splits the CCA into ECA (external carotid artery) and ICA (internal carotid artery). A second ligation was positioned around the ECA distal to the bifurcation. A vascular clamp (FST) around the ICA prevented backflow from the distal vasculature when a microincision into the CCA with spring scissors (FST) was made for the induction of an MCAO suture (9-10 mm coating length, 0.19 ± 0.01 mm tip diameter, Doccol). After removal of the clip, the filament was pushed forward until it occluded the MCA (middle cerebral artery). At this position, it was fixed with an extra suture around the CCA (Figure 2-1) that served for the permanent middle cerebral artery occlusion (pMCAO) for the next 4 hours. The application of Xylocain Gel 2 % (AstraZeneca GmbH) prevented wound pain.

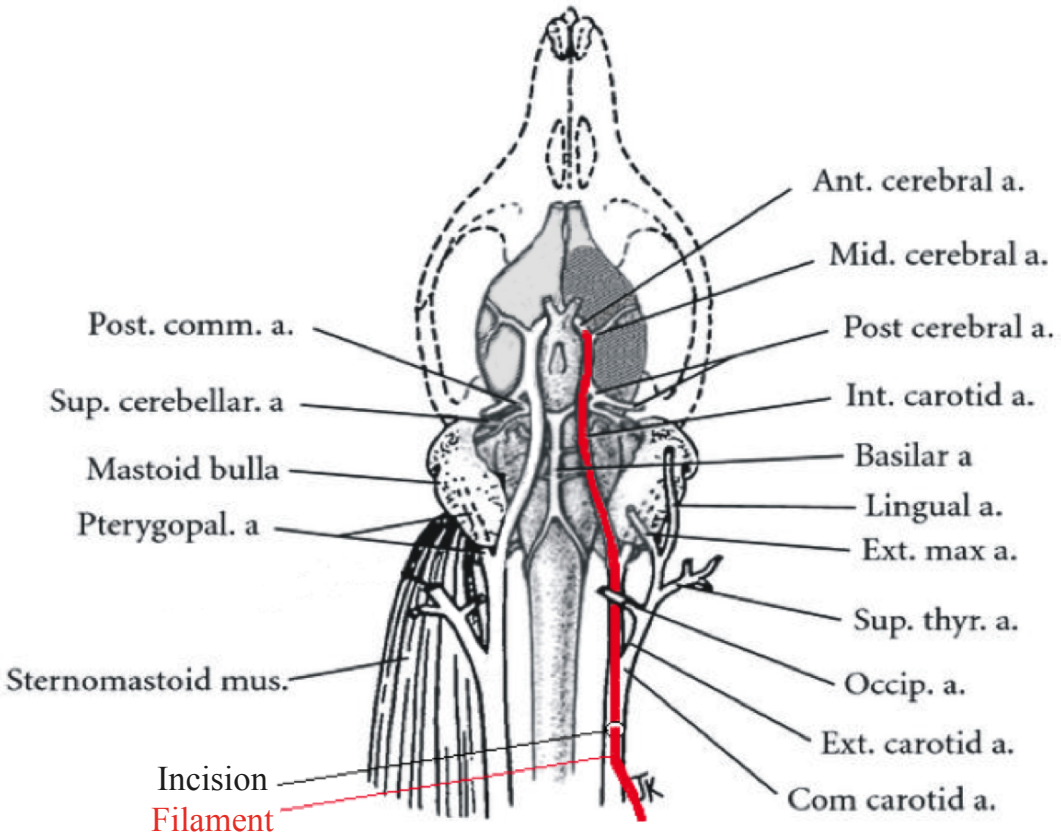

Figure 2-1: Schematic illustration of a mouse head from basal view during middle cerebral artery occlusion. During surgery, the filament (red) is inserted through an incision into the CCA and pushed forward where at its final position the MCA is occluded. (Adapted with permission from Lippincott Williams and Wilkins/Wolters Kluwer Health: Longa et al., 1989.)

The stroke model pMCAO induced left cerebral ischemia and was performed after the cranial window preparation. After the induction of pMCAO, the implanted cranial window enabled the investigation of PIDs for up to 4 hours (either by laser speckle contrast imaging, electrophysiology or 2-P imaging).

Before pMCAO induction and at the end of experiments, blood oxygenation values and heart and breathing rates were monitored by pulse oximetry using a MouseOx Plus Non Invasive Vital Signs Monitor coupled to a Mouse Thigh Sensor (Starr Life Sciences corp.).

2.3.2 Cranial Window Preparation

Anesthesia was induced with 3 % isoflurane (Forene, AbbVie) in pure oxygen (v/v) and maintained at 1-1.5 % isoflurane with a face mask while keeping the mouse on a heating pad (FST) at 37 °C. A drop of Bepanthen (Bayer) prevented the eyes from drying out. After subcutaneous injection of 200 µl local anesthetic Xylocain (2 % dental with adrenalin, Densply), the scalp was removed. A metal plate was fixed on the skull with dental cement (Cyano Veneer and Cyano Fast, Hager & Werken) and placed in a stereotactic frame. Cranial windows were implanted over the primary somatosensory cortex of the left hemisphere, centered at stereotactic coordinates 2.5 mm lateral and 1.5 mm posterior to bregma (Dong, The Allen Institute for Brain Science, 2008). The dura mater was pulled apart with a bent 20 G cannula if necessary for electrode insertion or for blocker application. Small bleedings were stopped using a piece of Spongostan Standard (Ethicon). For electrophysiology, windows were temporarily covered with a glass coverslip before pMCAO induction, and therefore fastened with Kwik-Cast Silicone Elastomer (WPI). For 2-P imaging, the windows were covered with 1.5 % agarose in ACSF to avoid movement artifacts during imaging and sealed with a glass coverslip.

To visualize calcium activity in astrocytes during 2-P imaging, the calcium-sensitive dye Oregon Green 488 BAPTA-1 AM (OGB-1) was injected into the cortex by multicell bolus loading (Stosiek et al., 2003) during cranial window preparation. Before injection, OGB-1 was solubilized in 20% Pluronic and 80% DMSO (Life Technologies) and diluted to 1 mM with PBS. Pipettes with a tip diameter of 4-6 µm were backfilled with this solution and lowered into the cortex to a depth of 80-130 µm (directing neuronal layers 2/3). The dye was pressure-injected with a microinjector at 0.2-0.5 bar for 30-60 seconds (Figure 2-2). In some experiments, in which CFP-positive animals were not available, mice were co-injected with 100 µM sulforhodamine 101 (SR101, red, Sigma) during OGB-1 injection that enabled the identification of astrocytes at wavelengths longer than 585 nm. The cover glass (diameter 3 mm) was mounted on top of 1.5 % agarose, dental cement sealed its rim to stabilize the window during imaging.

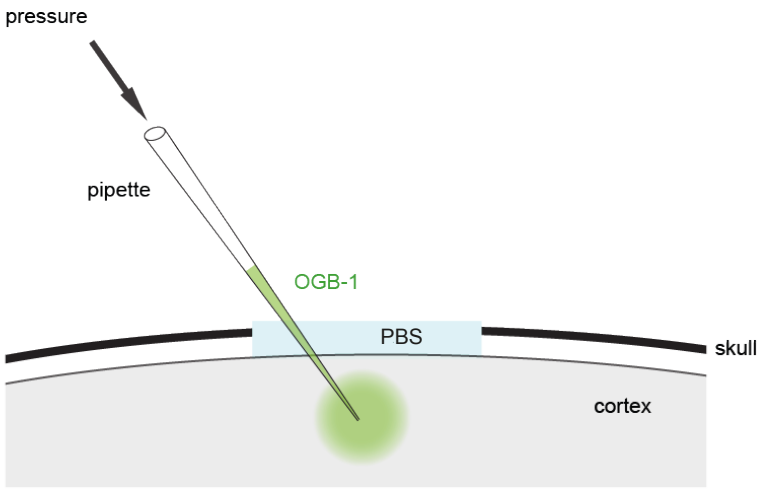

Figure 2-2: Schematic illustration of Oregon Green 488 BAPTA-1 AM (OGB-1) pressure injection. The pipette was filled with the calcium indicator OGB-1 diluted in PBS or sulforhodamine 101 and was inserted into the cortex. Pressure application of 0.2–0.5 bar allowed injection of the dye into neuronal layers 2/3.

2.3.3 Two-Photon Microscopy

After cranial window preparation and injection of the indicator (2.3.2), the anesthetized mouse was placed in a stereotactic frame under an upright 2-P microscope (LaVision Trim ScopeII) with a 20x/1.0 NA objective (Zeiss). For 2-P imaging, fluorophores were excited with a titanium/sapphire laser (Coherent), tuned to 880 nm. Over a scan field of 250 x 250 µm, three non-descanned detectors (NDDs) collected the emitted light in a range of 460-500 nm (CFP), 505-565 nm (OGB-1), and 635-675 nm (Alexa Fluor 633) respectively wavelengths longer than 585 nm (SR101, Texas Red dextran). The mouse was temporally taken out of the frame for pMCAO induction (2.3.1).

For imaging the Ai38 mouse line, the laser wavelength was tuned to 900 nm and emitted light collected in a range of 500-520 nm (GCaMP3).

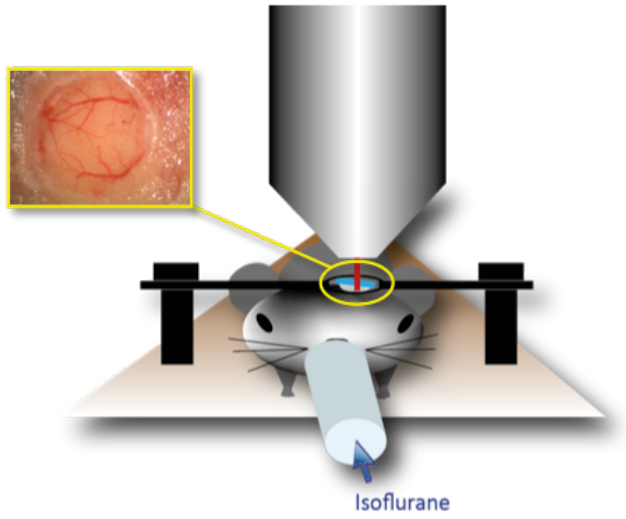

Figure 2-3: Scheme of a mouse fixed in a stereotactic frame with an implanted cranial window. During 2-P imaging, the mouse is placed on a heating pad and anesthesia is maintained by inhalation of isoflurane. The objective is positioned above the cranial window (yellow circle) for 2-P imaging. The magnification (left) shows a photograph taken from the top of a cranial window where pial vessels are visible under the sealed coverslip.

Before pMCAO induction, IV injection of Alexa Fluor 633 Hydrazide (Life Technologies) enabled the differentiation of arteries and veins under the 2-P microscope. After scanning the cranial window through a 655/20 BP filter, a penetrating artery labeled with Alexa 633 was centered in an imaging field of 250 µm x 250 µm. Subsequently, the blood plasma was labeled by Texas Red 70 kDa dextran (Life Technologies) IV injection. A Z-Stack of the CFP signal at 2 µm Z increments with XY resolution of 2.0 pixel/µm represented the baseline data for astrocyte edema measurement. A line scan (585+ nm) was taken with 500 Hz over 30 s, following a Texas Red labeled cortical capillary longitudinally over 30 µm. The mice were then taken out of the frame for pMCAO induction (2.3.1) and placed back under the microscope. In time-lapse series, fluorescence intensity was recorded in a depth of 100-150 µm (neuronal layers 2/3) with 3 Hz and a spatial resolution of 1.0 pixel/µm. Thereby, a PID was identified from the OGB-1 signal in form of a neuroglial calcium wave of typical velocity. Two minutes after the first PID became visible, the Z-Stack was repeated to capture CFP fluorescing astrocytes for edema measurement. A second line scan showed the reduction of CBF characteristic for the penumbra (60-80 %).

2.3.4 Laser Speckle Contrast Imaging

After cranial window preparation (2.3.2), the mouse was transferred into a stereotactic frame, which was placed under the laser speckle PeriCam PSI (Perimed) device. Cortical CBF in the anesthetized mouse was measured with the appropriate software PimSoft (Perimed) with a resolution of 60 µm/pixel. After baseline CBF recording for 5 minutes, the mouse was taken out for pMCAO induction (2.3.1) and placed back into the frame for further CBF monitoring over 4 hours. Laser speckle contrast imaging is based on the scattering of a laser beam by moving objects (e.g. blood cells); the estimated pattern is inversely proportional to perfusion (Dunn, 2011).

2.3.5 Electrophysiology

After cranial window preparation (2.3.2) and pMCAO induction (2.3.1), the anesthetized mouse was transferred into a stereotactic frame within a Faraday cage. A pipette puller (PC-10, Narishige) was used to pull a glass pipette with 2-5 µm tip diameter out of a Borosilicate Glass Capillary (WPI), which was filled with PBS. An Ag-AgCl electrode (Warner Instruments) was inserted into the pipette and connected to a head stage (EXT-02, npi). A micromanipulator (Harvard Apparatus) was used to position the pipette into the cortex at an angle of 50°. A reference Ag-AgCl electrode pellet (WPI) was placed into the neck tissue and also connected to the headstage. Finally, the cranial window was covered with 1.5 % agarose in ACSF and a glass coverslip. The direct current (DC) potential was amplified (100 x) and the signal filtered at 3-30 Hz by an EXT-02F/2 amplifier (npi), eliminated from noise with a Hum Bug device (Quest Scientific), and recorded by a MICRO 2 1401 data acquisition unit (CED), which was connected to a PC. For laser Doppler flowmetry (LDF), an optic fiber was placed in 3-5 mm distance to the electrode above the same hemisphere. A flowmeter (VMF-LDF2, Moor) focused a laser beam of a certain wavelength onto the skull, under which moving blood cells caused a Doppler shift in the backscattered light beam proportional to blood cell velocity (Dirnagl et al., 1989). Noise was eliminated by a second Hum Bug and recorded in a second channel of the data acquisition unit. For the first 4 hours of pMCAO,

DC potential and LDF were monitored while the mouse was constantly supplied with a low dose of isoflurane (0.8-1.2 %).

2.3.6 Immunofluorescence

After transcardial perfusion at 4 °C with 4 % paraformaldehyde (16 % PFA, Thermo Scientific, diluted in PBS), brains were post-fixed over night and stored in 15 %, then 25 % D-Glucose (Sigma) diluted in PBS with 0.01 % (v/v) sodium azide (NaN_3, Roth) at 4 °C. After cryopreservation, 20 µm coronal slices were cut on a cryostat (Leica). Slices were mounted on Superfrost Plus slides (Menzel) and blocked with 5 % goat serum (Vectra) in 0.25 % Triton X-100 (in PBS) for 60 minutes. Primary antibodies 1) rabbit (rb) anti-GFP (Invitrogen, 1:1000), 2) mouse (ms) anti-S100β (Sigma, 1:1000), and 3) rat anti-GFAP (Invitrogen, 1:1000) were diluted in blocking solution and incubated on the slides over night. After washing, the secondary antibodies Alexa 488 anti-rb, Alexa 555 anti-ms, and Alexa 633 anti-rat (Life Technologies, 1:1000 diluted in PBS) were applied for 2 hours. After washing, slides were dipped in Hoechst 33258 (10 µg/ml PBS, Life Technologies) for 3-5 seconds and washed in water, mounted with DePeX (Serva) containing Dabco (1 mg/ml, Sigma), and coverslipped (Menzel). By laser scanning microscopy (Zeiss LSM 700), tile scans over a total hemisphere or only over the hippocampus were taken with a 20x/0.8 NA objective (Zeiss). Subsequently, GCaMP3 expression was quantified in astrocytes as the ratio of GFP- and S100β-positive to the number of all S100β-positive astrocytes if the nucleus was labeled with Hoechst 33258.

2.3.7 Cre/loxP System

Genetic reporter mice of the line Ai38 express GCaMP3 in a Cre-dependent manner: The strong CAG promoter at the Rosa26 locus only drives the expression of GCaMP3 after the deletion of a preceding Stop-codon by Cre-recombinase (Cre-ERT2) (Zariwala et al., 2012). The CreERT2 expression is controlled by a cell type specific promoter and is activated by tamoxifen-induction (Hayashi and McMahon, 2002). I intended to induce GCaMP3 specifically in astrocytes. The two different promoters Cx43 (Connexin 43) and

GLAST (glutamate transporters) in the cortex are solely expressed in astrocytes and were hence used for CreERT2 expression (Mori et al., 2006; Koulakoff et al., 2008). The Ai38 reporter mouse line was crossbred with Cx43-CreERT2 mice (Eckardt et al., 2004) (Cx43-CreERT2:Ai38) and GLAST-CreERT2 mice (Kang et al., 2010b) (GLAST-CreERT2:Ai38). Once Cre-ERT2 is induced in these mice, GCaMP3 is permanently translated in all astrocytes that expressed Cx43 respectively GLAST by the time of tamoxifen administration. For testing the efficiency of the two different astrocytic promoters in the Ai38 mouse lines, the GFP component of GCaMP3 was stained with immunofluorescent antibodies and their signals detected in a laser scanning microscope (LSM). The more efficient mouse line was used for 2-P imaging of pMCAO, whereby I intended to test this astrocyte-specific Cre/loxP system for its compatibility for imaging astrocytic calcium during PIDs.

2.3.8 Genotyping

Genotyping was carried out with genomic DNA from tail or ear biopsies after lysis with DirectPCR Lysis Reagent Tail (Peqlab, Germany). Primers used for genotyping are listed in Table 2. For the Cx43-CFP allele, KAPA Mouse Genotyping Hot Start Kit (Peqlab, Germany) was used for initial denaturation at 95 °C for 180 sec, 30 repeats at (94 °C for 30 sec, 63°C for 30 sec, 72 °C for 45 sec), and final elongation at 72 °C for 300 sec. PCRs for IP3R2 alleles were run separately with Platinum Taq DNA Polymerase (Life Technologies GmbH, Germany) and 50 mM $MgCl_2$ (Thermo Scientific, Germany) at 95 °C for 180 sec, 35 x (94 °C for 30 sec, 63 °C for 30 sec, 72 °C for 45 sec), and at 72 °C for 300 sec. PCRs for Trpv4 genotyping were done with Platinum Taq DNA Polymerase (Life Technologies GmbH, Germany) and 50 mM $MgCl_2$ at 94 °C for 300 sec, 30 x (94 °C for 45 sec, 68 °C for 90 sec, 72 °C for 150 sec), and at 72 °C for 600 sec. Aqp4 genotyping was also done using KAPA Mouse Genotyping Hot Start Kit at 95 °C for 180 sec, 35 x (95 °C for 15 sec, 57 °C for 15 sec and 72 °C for 10 sec), and at 72 °C for 300 sec. Both Cx43-Cre and GLAST-Cre were genotyped with HotStarTaq Plus Master Mix Kit (Quiagen, Germany) at 95°C for 300 sec, 35 x (94 °C for 30 sec, 51.7 °C for 45 sec, 72 °C for 30 sec), and at 72 °C for 600 sec. Ai38 genotyping was carried out separately

for different primer pairs with HotStarTaq Plus Master Mix Kit at 94 °C for 300 sec, 4 x (94 °C for 30 sec, 60 °C for 45 sec, 72 °C for 45 sec), 34 x (94 °C for 30 sec, 55 °C for 45 sec, 72 °C for 60 sec), and at 72 °C for 600 sec.

Table 2: List of primers.

allele	sense	antisense	product
Cx43-CFP	GCACTTGGTAGGTAGAGCCTGTCAGGTC	AAGAAGTCGTGCTGCTTCATGTGG	500 bp
IP3R2-wt	ACCCTGATGAGGGAAGGTCT	GATCGATTCATAGGGCACACC	220 bp
IP3R2-ko	AATGGGCTGACCGCTTCCTCGT	TCTGAGAGTGCCTGGCTTTT	320 bp
Trpv4-wt	CATGAAATCTGACCTCTTGTCCCC	TTGTGTACTGTCTGCACACCAGGC	2.1 kbp
Trpv4-ko			1.1 kbp
Aqp4-wt	ACC ATA AAC TGG GGT GGC TCA G	TAG AGG ATG CCG GCT CCA ATG	260 bp
Aqp4-ko	ACC ATA AAC TGG GGT GGC TCA	CAC CGC TGA ATA TGC ATA AGG CAG	320 bp
Cx43/GLAST-Cre	GCGGTCTGGCAGTAAAAACTATC	GTGAAACAGCATTGCTGTCACTT	100 bp
Ai38-wt	CCAAAGTCGCTCTGAGTTGTTATC	GAGCGGGAGAAATGGATATG	604 bp
Ai38-fl	CTTCAAGATCCGCCACAACATCG	TTGAAGAAGATGGTGCGCTCCTG	546 bp

2.3.9 Buffers and Solutions

PBS:

- NaCl 0.8 g
- KCl 0.5 g
- Na_2HPO_4 1.44 g
- KH_2PO_4 0.24 g
- Fill up with distilled water to 1000 ml.

ACSF (10 x stock):

- NaCl 77,1 g
- KCl 2,2 g
- $MgCl_2$ 1,32 g
- $CaCl_2$ 2,21 g
- Urea 4,02 g
- Fill up with distilled water to 1000 ml.

For 100 ml ACSF take:

- Stock solution 10 ml
- Distilled water 90 ml
- $NaHCO_3$ 0.0207 g
- Glucose 0.067 g

TAE Buffer (50 x):

- Tris base 242 g
- Acetic acid 57.1 ml
- EDTA (0.5 M) 100 ml
- Fill up with distilled water to 1000 ml.

2.4 Data Analysis and Statistics

2.4.1 Two-Photon Data Analysis

Calcium signals from the OGB-1 signal were differentiated regarding their cell-specific origin using astrocyte labeling. After stabilization in Fiji (Schindelin et al., 2012), the CFP respectively SR101 signal of the time-lapse series was used to mark astrocytes in a set of regions of interest (ROIs). By excluding these astrocyte ROIs on the according stabilized OGB-1 recording, a separate set of neuronal ROIs was gained from the remaining labeled cell bodies. A Fiji macro (Image and Data Analysis Facility (IDAF), DZNE) extracted total intensity

values of the calcium signal within these two sets of ROIs for single astrocytes and neurons. A MATLAB script (IDAF, DZNE) extracted and normalized these calcium data as ΔF/F% after removing outliers with a median filter (window size: 5) and smoothing the signal with a Gaussian filter (window size: 8). Finally, the script analyzed peaks of the calcium signal. Thereby, a peak was considered as a calcium event if the first derivative of ΔF/F% exceeded 2 x SD of its baseline (time point of peak onset) using 100 data points (33 s) before peak onset as baseline. Peaks were analyzed regarding their amplitude (ΔF/F%), full duration of half maximum (FDHM), and time to peak (TTP). The velocity of a calcium wave was calculated by subtracting the time points of peaks from two ROIs with a distance of ≥ 100 µm.

During imaging, the blood plasma was labeled with Texas Red dextran. Erythrocyte velocity and flux were measured from line scans, i.e. repetitive scans over 30 s along the longitudinal axis of capillaries (over 30 µm) before and after pMCAO (Kleinfeld et al., 1998). In a line scan image, erythrocytes are visible as moving shadows in the stained blood plasma and appear as dark bands with a slope. Briefly, both the slope and the distance between the black bands are inversely proportional to the velocity of erythrocytes (Petzold and Murthy, 2011). The velocity was calculated from the angle of the bands with a MATLAB routine (provided by Schaffer-Nishimura Lab, Department of Biomedical Engineering, Cornell University). The flux was calculated from the number of bands within 30 sec after binarization of data using Fiji (Version 2.2.0-rc-241.49m). The CBF reduction after pMCAO was used to confirm that 2-P imaging took place in the penumbra.

For CBF measurement from the time-lapse series during the first PID, the recordings of the Texas Red signal were stabilized and resized in Fiji to 5 pix/µm. After 3D smoothing with a Gaussian filter (window size: 5), the diameter change of a penetrating arteriole during a PID was calculated over time with a MATLAB routine (IDAF, DZNE).

The blue fluorescent cytosol of CFP-positive astrocytes in Cx43-CFP enabled the differentiation of astrocytes from neurons and the calculation of edema formation, by measuring volumes of astrocytic somata before pMCAO and after PID. Using their CFP fuorescence in the two Z-stacks, astrocytes were

identified and 3D-reconstructed by Imaris Software (Bitplane). At the second time point, same cells were relocated by means of shape and spatial location, so that their volume could be tracked over time. Volume increases were measured by applying a MATLAB routine on Imaris (IDAF, DZNE). Edema formation (volume increase) in astrocytes of 100-1000 μm^3 size was determined by subtracting baseline cell volumes (pre-MCAO) from cell volumes 3-5 min after detection of the first PID (post-PID).

2.4.2 Laser Speckle Contrast Data Analysis

Data were analyzed after experiments by placing circular regions of interest (ROIs) over different cortical regions. ROIs 1-10 ($\approx$ 0.1 mm^2 each) reflected different regions from medial to lateral within the cranial window ($\approx$ 10 mm^2). The mean of pre-MCAO values in each ROI over 5 minutes represented the baseline value. The first 30 seconds of the post-MCAO measurement were defined as TOI (time of interest) 1. 30 seconds after approximately 1 hour of occlusion served as TOI 2. The last 30 seconds of the 4 hours post-MCAO measurement were regarded as TOI 3 and represented the residual CBF value at the end of the experiment. If PIDs occurred within one of the TOIs, the TOI was changed to a time point of a steady CBF level. 1 − CBF (TOI 1) was normalized to the corresponding baseline CBF (pre-MCAO) representing CBF reduction by pMCAO induction. 1 − CBF (TOI 2) and 1 − CBF (TOI 3) were also normalized to CBF (pre-MCAO) representing CBF reduction after 1 and 4 hours, respectively. TOI values were then compared between different ROIs.

2.4.3 Analysis of Electrophysiological Data Analysis

DC potential and CBF values deriving from LDF were both recorded with Spike 2 (CED software). A drop in the DC potential ($\geq$ 1 mV) indicated depolarization and was counted as a PID if it was accompanied by a CBF increase, indicating the CBF response to spreading depolarization. Further analysis included cumulative as well as averaged area under the curve (AUC), latency to first PID, amplitude, time to peak (TTP), total number of PIDs,

number of PIDs during the 1st and 2nd hour, and number of PIDs during 3rd and 4th hour (Figure 2-4).

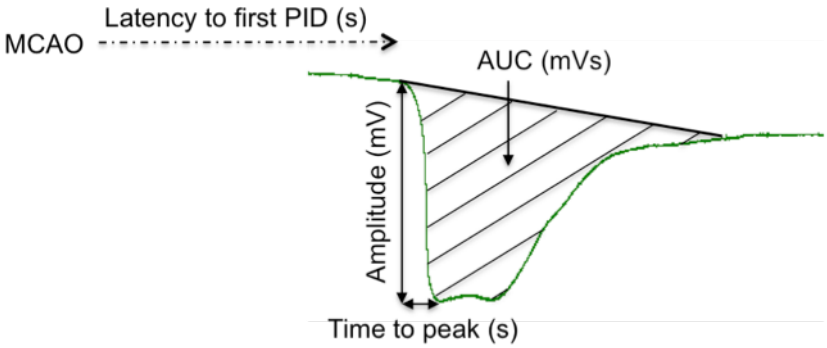

Figure 2-4: Parameters used for PID analysis of DC potential measurement. AUCs of single PIDs (Vs) over the total measurement time of 4 hours were summed for cumulative AUC or averaged for average AUC. Latency to first PID (s), amplitude (mV), time to peak (s), as well as the number of PID incidences within 4 hours (not shown here) are compared between the different groups.

2.4.4 Statistics

Graph Pad Prism 6.0e was used for statistical analysis. Statistical significance between two groups was determined by Mann Whitney test, except for edema measurements, where a paired t test after D'Agostino & Pearson omnibus normality test was used. Significance between more than two groups was tested with Kruskal-Wallis test followed by Dunn's multiple comparisons test. Data are presented as mean ± standard error of the mean (s.e.m.). A p value less than 0.05 was considered as statistically significant.

3 Results

3.1 Identification of the Penumbra with Laser Speckle Contrast Imaging

I prepared cranial windows above the left motor cortex of wildtype mice (n = 4). In different regions of interest (ROIs) within the cranial windows (ROIs 1-10, from medial to lateral), I measured the cortical microcirculation (relative cerebral blood flow, CBF) before and during pMCAO by laser speckle contrast imaging. ROI positions are marked by circles in representative images in Figure 3-1 A.

Before pMCAO induction, baseline CBF was measured within each ROI. After pMCAO induction, CBF was monitored again in each ROI and PIDs were recorded over 4 hours, based on their typical CBF signature consisting of hypoperfusion followed by hyperperfusion (arrows in Figure 3-1 B). Colored graphs represent microcirculation within ROI 1 (blue), ROI 5 (red), and ROI 10 (green) relative to baseline CBF before pMCAO within the same ROI. ROI 1 (blue) is located most medially, ROI 10 most laterally within the cranial window, and ROI 5 is located in between (compare Figure 3-1 A). As noted above, a PID was identified by a sudden temporal CBF decrease followed by a temporal increase. Vertical blue lines in Figure 3-1 B show the exemplary positioning of TOIs 1-3 for subsequent analysis of CBF reduction directly after pMCAO induction, after 1 hour, and after 4 hours.

CBF values in ROIs 1-10 at different time points (TOIs 1-3) are presented as bar diagrams in Figure 3-1 C and are also listed in Table 3 (Appendix). These CBF values are presented relative to baseline, which was defined as CBF before pMCAO induction. I observed a decrease of residual CBF in each ROI from

TOI 1 to TOI 2 that remained constant from TOI2 to TOI 3. Moreover, residual CBF values that usually indicate the penumbra (20-40 %) (Hossmann, 1994b) could be found between ROI 5 (36,8 ± 6,1 %) and ROI 10 (22,6 ± 4,4 %) in my model.

In summary, I detected spontaneous PIDs with laser speckle contrast imaging, visible as temporal CBF decreases and increases. Furthermore, I defined the region between ROI 5 and 10 as infarct penumbra, characterized by residual CBF values of 20-40 % after 1 hour, positioned 2.5-3 mm lateral and 1.5 mm anterior to the bregma. Consequently, this region was later investigated using electrophysiological and 2-P measurements.

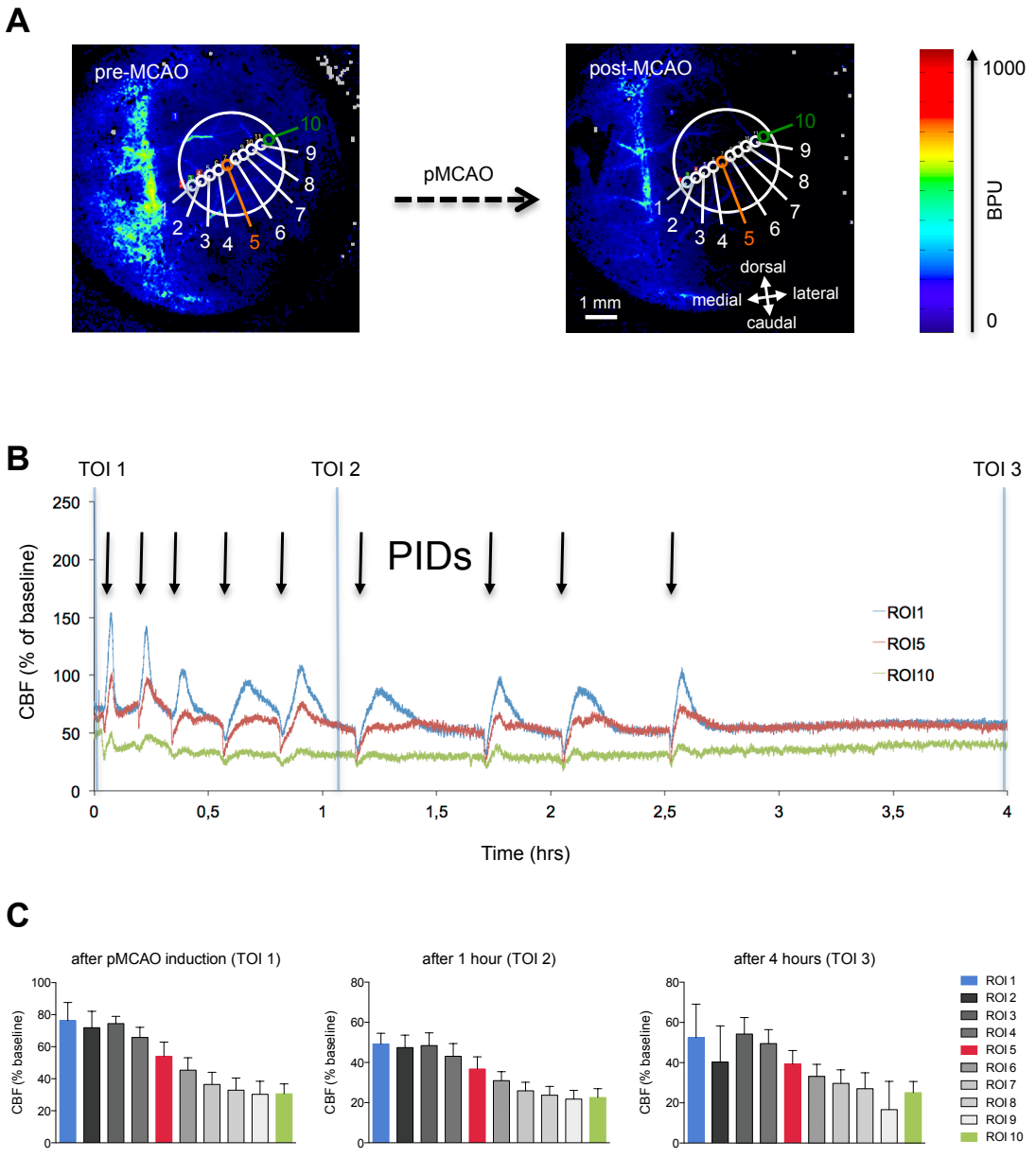

Figure 3-1: Laser speckle contrast imaging in different regions of the cranial window after pMCAO. A) Heat maps of cortical microcirculation in relative blood perfusion units (BPU) measured with laser speckle above the left hemisphere before (left) and after (right) pMCAO (with Pimsoft, Perimed). ROIs 1-10 from medial to lateral (small circles), positioned above the cranial window (large circles). B) Microcirculation within the cranial window: CBF in ROI 1, 5, and 10 over 4 hours (post-MCAO), normalized to their specific baseline CBF over 5 min (pre-MCAO). PIDs (arrows) are characterized by a sudden CBF decrease followed by temporal CBF increase. TOIs 1, 2, and 3 (blue bars) show different time points. TOI 1: directly after pMCAO induction, TOI 2: after approx. 1 hour, TOI 3: after 4 hours. C) Bar diagrams of residual CBF at ROI 1-10 during TOI 1 (left), TOI 2 (middle), and TOI 3 (right) normalized to baseline CBF. Data are represented as mean ± s.e.m..

3.2 Electrophysiological Measurements of PIDs

To investigate the electrophysiological characteristics of PIDs, I prepared a cranial window above the region that was defined as penumbra with laser speckle contrast imaging. Subsequently, I induced a pMCAO and measured the DC potential during spontaneously occurring PIDs with an intracortical electrode at a depth of ~100 µm for a total of 4 hours. In parallel, I monitored CBF by LDF in 3-5 mm distance to the electrode in order to verify the propagating nature of PIDs.

After pMCAO induction, a PID was associated with a characteristic temporary reduction of the DC potential that was followed by an increase of CBF. A representative example of LDF and DC potential changes during a PID over a period of 500 s is shown in Figure 3-2. The electrophysiological characteristics of PIDs will be reported in the subsequent paragraphs.

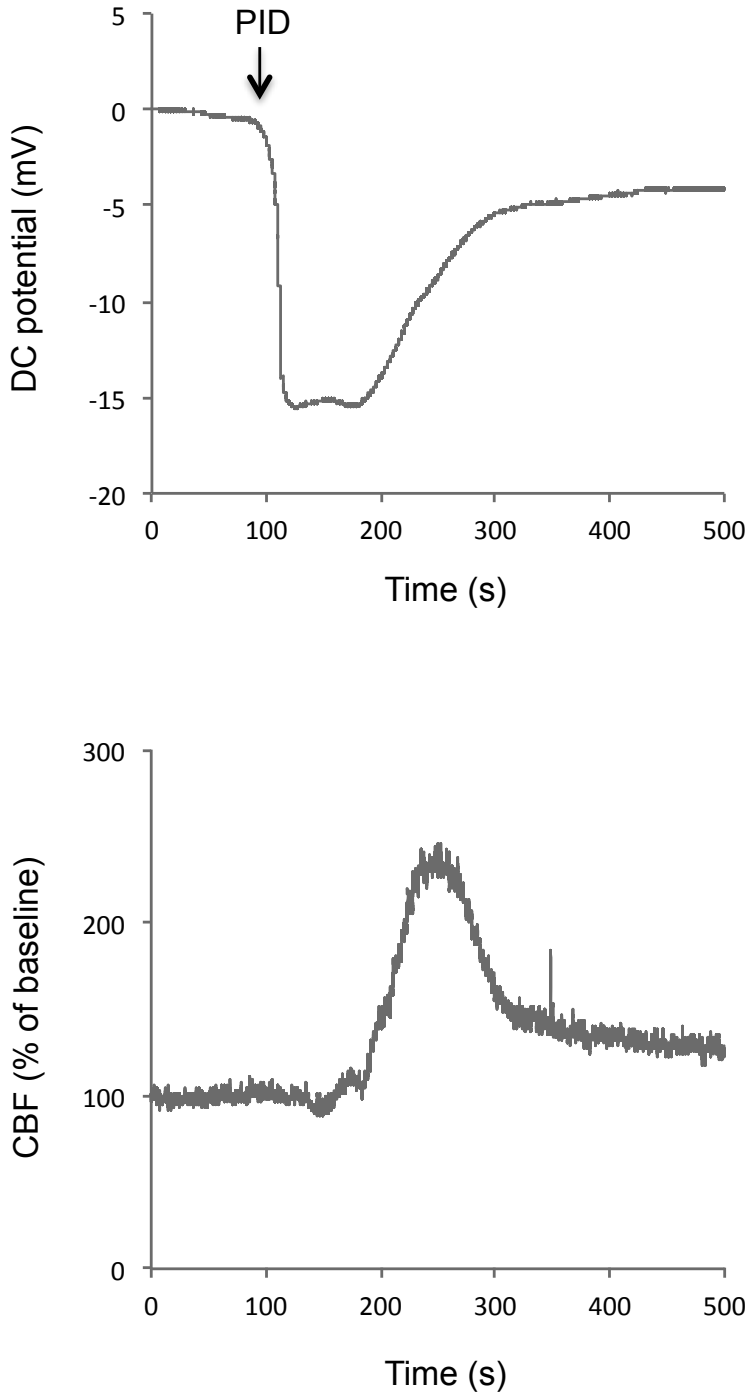

Figure 3-2: DC shift in the penumbra and distant CBF change during a PID. Representative example of a PID over 500 seconds, measured with an intracortical electrode and laser Doppler flowmetry in 3-5 mm distance: A negative shift of the DC potential (upper graph; amplitude: -15 mV) is followed by a delayed relative CBF increase (lower graph, here: 140 % increase compared to 100 % baseline), demonstrating the propagating nature of the event. Note that the LDF probe was placed over healthy cortex outside of the penumbra, and therefore shows changes typical of a normoxic spreading depolarization.

3.2.1 IP3R2 Deletion Reduces PID Occurrence and Increases Latency to First PID

Using the electrophysiological setup described above, different groups were compared to their respective controls:

- IP3R2-kos (n = 10) and TRPV4-kos (n = 7) vs. IP3R2/Trpv4-ctrls (n = 10).
- Aqp4-kos (n = 10) vs. Aqp4-ctrls (n = 10).
- HC-067047 (TRPV4 antagonist; n = 10), AqB013 (AQP4 antagonist; n = 10), and KB-R7943 (NCX antagonist; n = 10) vs. DMSO (n = 10).

The total PID number within 4 hours was significantly reduced by 55 % in the IP3R2-kos (1.3 ± 0.4 PIDs, p = 0.0233) compared to controls (2.9 ± 0.3 PIDs) (Figure 3-3 A). The latency to the first PID was 5.3-fold higher in IP3R2-kos (107.5 ± 26.4 min, p = 0.0064) compared to controls (20.3 ± 8.3 min) (Figure 3-3 B). Neither amplitude (Figure 3-3 C) nor time to peak (Figure 3-3 D) of the DC potential differed between any groups. Likewise, cumulative and average AUC of DC shifts showed no differences (Figure 3-3 E and F), although there was a trend towards a reduced cumulative AUC in IP3R2-ko mice that did not reach statistical significance.

No significant differences were observed in Trpv4-kos, Aqp4-kos, or mice treated with pharmacological antagonists compared to controls.

Taking a closer look at IP3R2-kos, the number of PIDs within 4 hours as a function of elapsed time (latency) is illustrated in Figure 3-4 A. A reduced number of PIDs at early time points in IP3R2-kos demonstrates the increased latency until occurrence of the first PID. The reduced frequency predominated within the 1st and 2nd hour: Reduction by 62 % in IP3R2-kos (0.8 ± 0.4 PIDs, p = 0.0030) versus controls (2.1 ± 0.3 PIDs), while 3rd and 4th hour showed no difference (Figure 3-4 B). Closer examination of the cumulative AUC of IP3R2-kos within the 1st and 2nd hour showed a trend toward a reduction that did not reach statistical significance (Figure 3-4 C).

In summary, the occurrence of PIDs within the first 2 hours of measurement was significantly reduced in IP3R2-kos while in the 3rd and 4th hours no difference to the control group were visible. In line with this, the latency to the first PID was significantly increased in the IP3R2-kos.

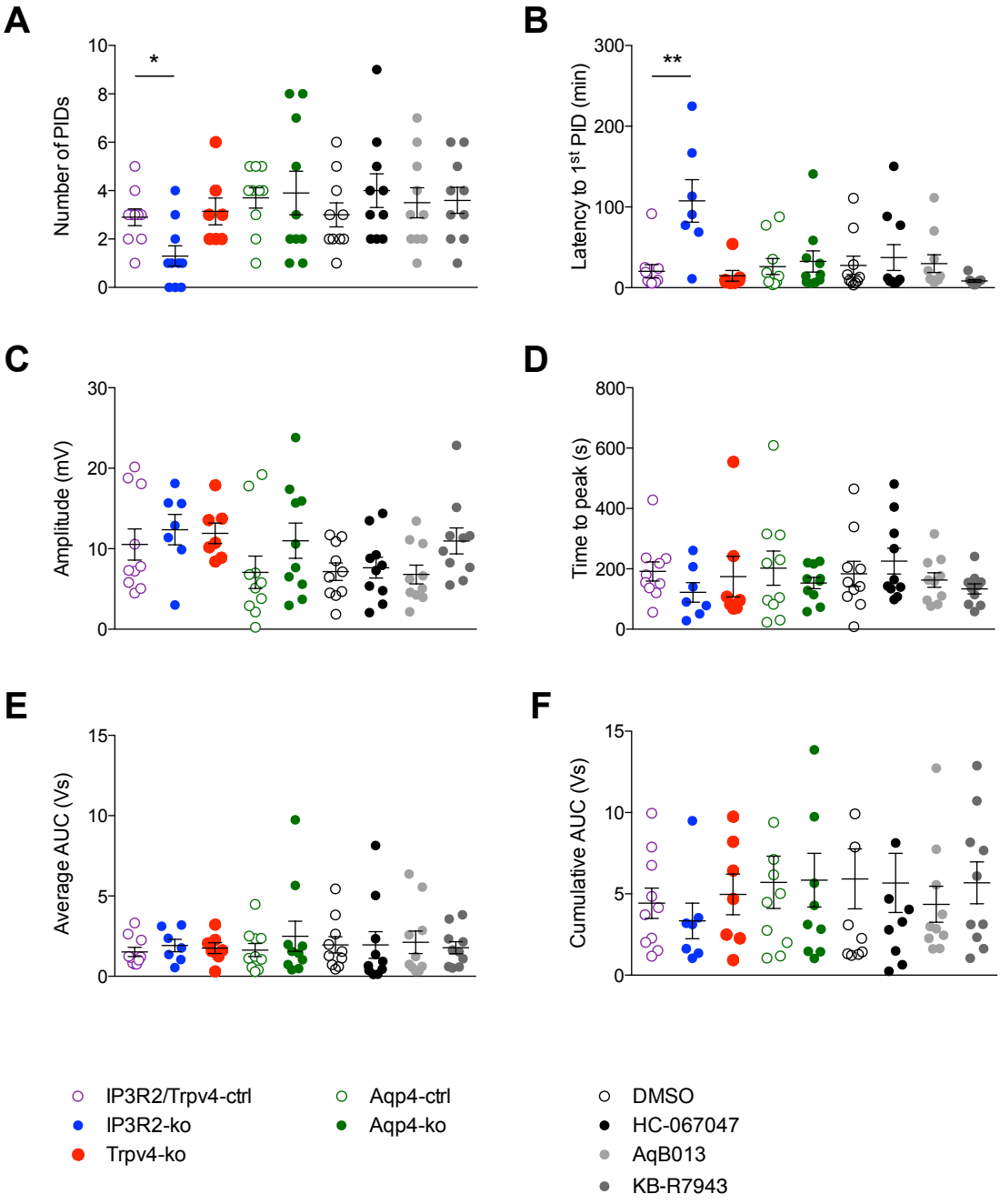

Figure 3-3: Analysis of detected PIDs in DC recordings. A) The numbers of PIDs within 4 hours show significant reduction for IP3R2-kos compared to their controls (IP3R2/Trpv4-ctrl). B) Also, the latency to the first PID is significantly reduced in the IP3R2-kos. C) Mean time to peak and D) mean amplitude of the PIDs show no alterations. E) Average AUC and F) cumulative AUC neither show differences. Data are represented as mean ± s.e.m.; * $p<0.05$, ** $p<0.01$, Kruskal–

Wallis test followed by Dunn's multiple comparisons test for comparison of 3 means or more, Mann-Whitney test for comparison of 2 means (Aqp4).

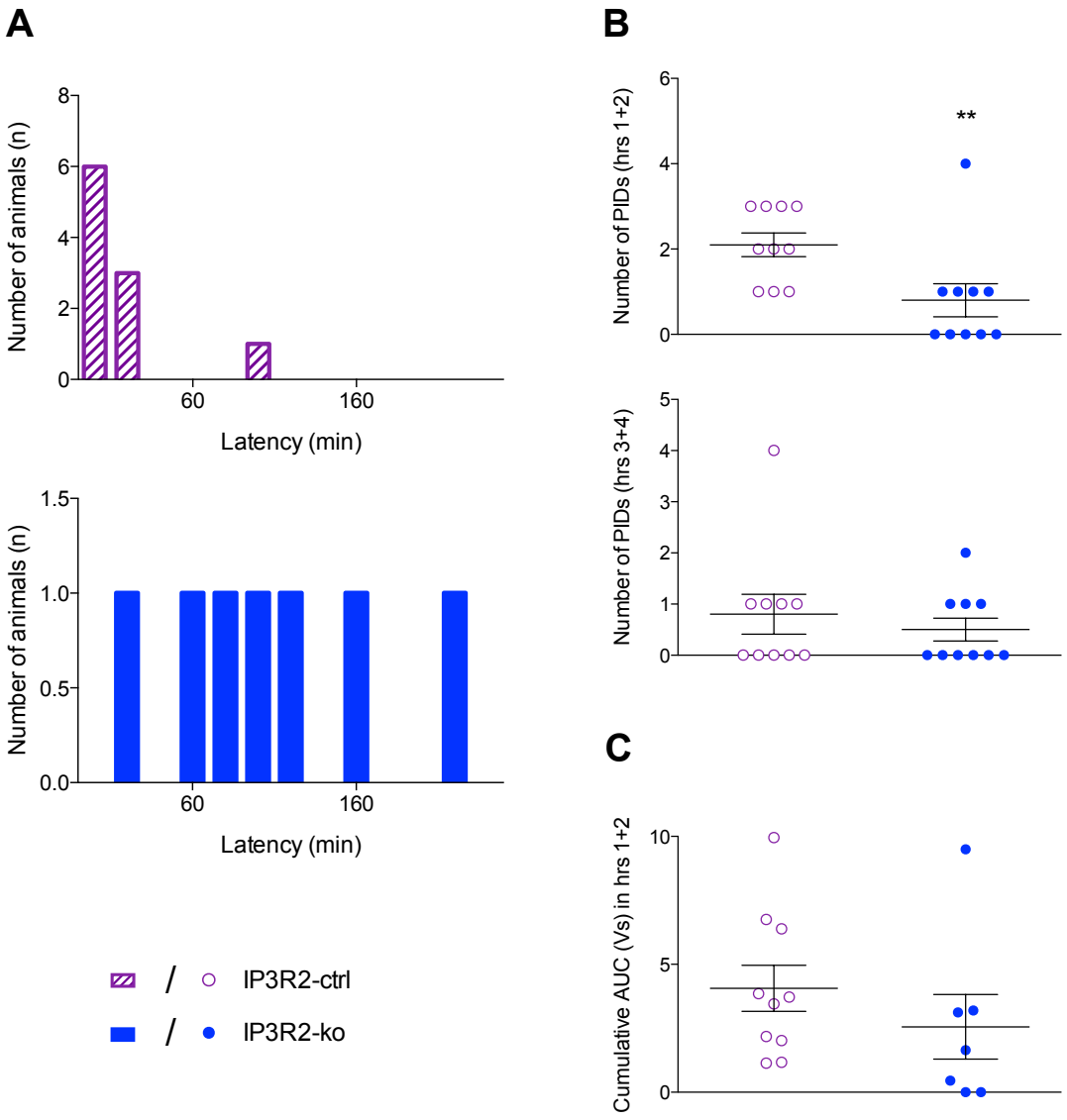

Figure 3-4: Delay and reduction of PID incidences in IP3R2-kos versus controls after pMCAO induction. A) Histograms illustrate first PID incidences in reference to the elapsed time in IP3R2/Trpv4-ctrls and IP3R2-kos, highlighting increased latency to the first PID in IP3R2-kos. B) Separated presentation of the 1st and 2nd hour (upper diagram) and 3rd and 4th hour (lower diagram) of the measurements highlight significant reduction of PID incidences in the IP3R2-kos within the first two hours of pMCAO. C) Cumulative AUC within the first 2 hours of measurement showed no differences. Data are represented as mean ± s.e.m.; ** $p<0.01$, Mann-Whitney test.

3.3 Two-Photon Microscopy

For 2-P imaging experiments, I injected a calcium indicator during cranial window preparation. The mouse was positioned under the 2-P microscope for cell volume and CBF baseline measurements (Z-Stack and line scan). Afterwards, the mouse was taken out for pMCAO induction and subsequently placed back under the microscope for further imaging of CBF, calcium, and cell volume.

3.3.1 Alexa Fluor 633 Labels Penetrating Arterioles

To ensure that I measured diameter changes of penetrating arterioles – and not of, e. g., venules – I injected Alexa Fluor 633 into the tail vein before pMCAO induction to fluorescently label arterioles (Shen et al., 2012). The two-photon imaging field was positioned so that a labeled arteriole was in the center of the field. In addition, I injected Texas Red dextran (70 kDa) into the tail vein before pMCAO to fluorescently label the plasma for subsequent CBF measurements. Measuring CBF before and after pMCAO confirmed that imaging took place in the penumbra and recording arteriolar diameter changes during PIDs indicated relative CBF changes.

A representative example of Alexa 633 and Texas Red dextran labeling in a cortical arteriole is given in Figure 3-5.

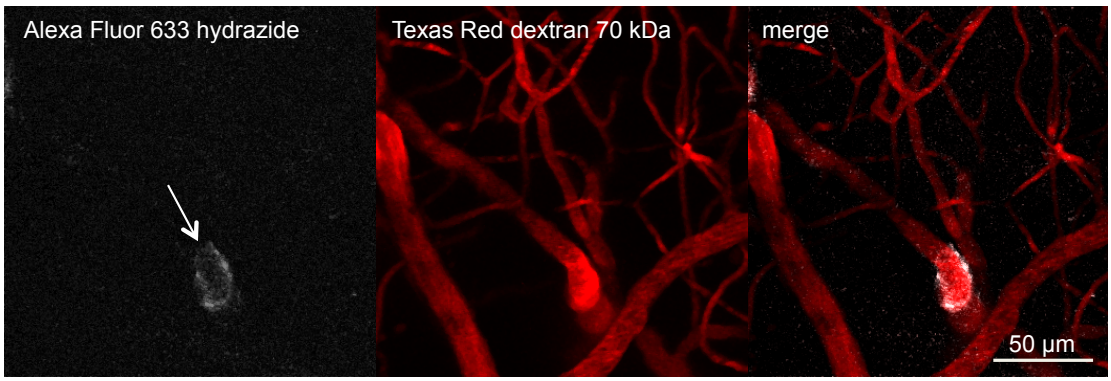

Figure 3-5: Identification of a penetrating arteriole in the cortical vasculature. Left: Alexa Fluor 633 Hydrazide labels elastin fibers of penetrating arteries after IV injection. The arrow shows the direction of the arteriole from surface to deeper layers. Middle and right: After subsequent injection of Texas Red dextran 70 kDa, the total vasculature is labeled in red and the arteriole is identified for further

CBF measurement. Images are 3D maximum projections from Z-Stacks over 200 µm cortical depth.

3.3.2 Simultaneous Imaging of CBF, Calcium, and Edema during pMCAO

The intention during 2-P imaging of pMCAO was to monitor CBF changes on the basis of arteriolar diameter changes, to obtain calcium signals from astrocytes and neurons, and to measure astrocyte edema at the same time. Therefore, differently fluorescing signals were separated by the aforementioned filter setup and collected by three different detectors (Figure 3-6). Texas Red dextran 70 kDa labels the vasculature (top left image) so that the plasma emits light in the red spectrum. Circular formations represent penetrating blood vessels from the top view (open arrow) while planar lines are small vascular branches, in which erythrocytes can be seen as black shadows (solid arrow). Green-emitting OGB-1 AM labels calcium in astrocytes and neurons (top right) while only astrocytes express blue-fluorescent CFP (bottom left image). The latter not only enabled differentiation of astrocytes from neurons, but also served as a basis for astrocyte edema calculation by volume estimation. The distribution of blood vessels, astrocytes, and neurons is represented in the merged image (bottom right): Vasculature is displayed in red, astrocytes in blue, and neurons in green. Astrocytic endfeet cover penetrating blood vessels, visible as blue rims around a red circle (open arrow).

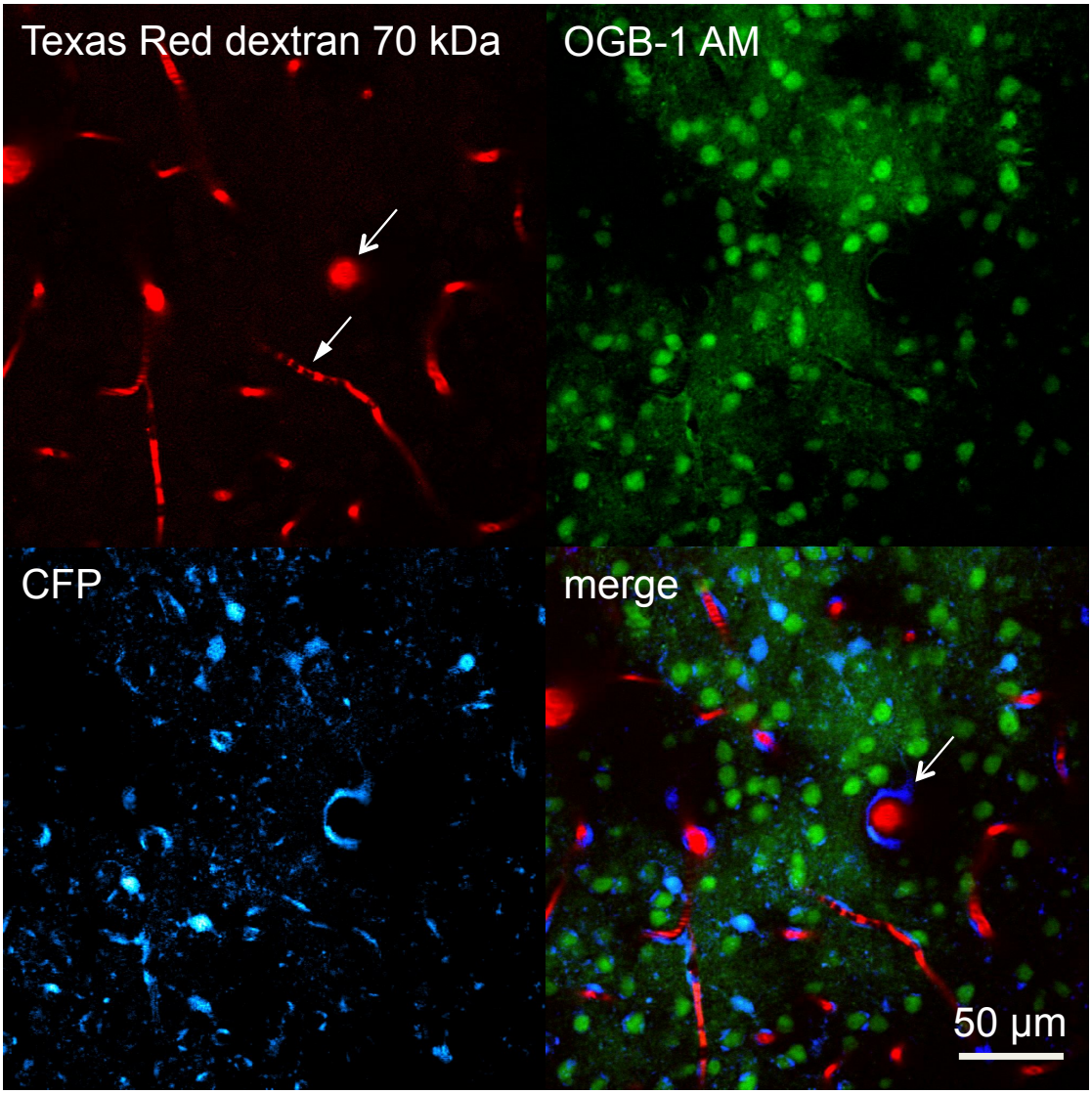

Figure 3-6: Simultaneous *in vivo* 2-P imaging of CBF, calcium, and edema in Cx43-CFP$^{+/-}$ mice. Top left: Texas Red dextran 70 kDa labeled the blood plasma for CBF monitoring during calcium imaging from line scans of capillaries (solid arrow) and time-lapse series from penetrating arterioles (open arrow). Top right: Oregon Green 488 BAPTA-1 (OGB-1) AM labels calcium in astrocytes and neurons. Bottom left: Endogenous expression of cyan fluorescent protein (CFP) in astrocytes by Cx43-CFP$^{+/-}$ mice for estimation of astrocytic volumes necessary for edema calculation. Bottom right: Merge demonstrates the differentiation of astrocytic and neuronal calcium signals and simultaneous CBF mesurement. Open arrow labels an astrocytic endfoot covering a penetrating artery. Images are taken from a single focal plane at -90 µm cortical depth.

3.3.3 Cerebral Blood Flow Measurement during pMCAO

Line scans of capillaries along the longitudinal axis were used to measure local CBF before pMCAO and after the first PID. An example is shown in Figure 3-7 A. The arrow indicates the scan path (top image). Along this scan path, repeated line scans (500 Hz) over 30 seconds show the movement of erythrocytes (black bands) through 20 µm of the capillary, depicted in a matrix with a spatial and a temporal dimension (bottom image). Before MCAO induction and after PID detection, velocity and flow rate were calculated from the slopes of non-fluorescent erythrocytes in the labeled blood plasma. The reduction of velocity and flux should be compatible with the penumbra, which is commonly defined as the infarct region with 60-80 % CBF reduction from baseline (Donnan et al., 2007). In this example, velocity was reduced from 2.24 to 0.89 mm/min (60.3 %). The flow rate decreased from 97 to 23 erythrocytes/s (76.3 %). In average, the residual velocity of erythrocytes measured from line scans after MCAO was 64.9 ± 12.4 % (Appendix, Figure 5-1). Therefore, CBF measurements fulfilled our pre-specified criteria of the penumbra.

During PIDs, no line scans could be performed, because edema led to movements in the Z direction (the capillary disappeared from the focal plane), and because time-lapse series were taken for calcium imaging (line scans could not be performed during time-lapse series). Instead, I estimated CBF changes during PID from diameter changes of penetrating arterioles (identified earlier by Alexa Fluor 633 labeling). Examples of the vasculature at baseline and during a PID are given in Figure 3-7 B. The calculated diameter over time (lower panel) shows the arteriolar constriction during a PID measured along the blue bars crossing the arteriole in the upper images.

In Figure 3-8, diameter changes by constrictions (left) and dilations (right) of different knockout-groups (A) and blockers (B) compared to the according controls are presented as bar graphs. Below the bars, the number of counted constrictions or dilations is given as a proportion of analyzed arterioles. For example, in IP3R2/Trpv4-ctrl mice, a constriction of 12.5 ± 1.4 % was detectable in 8 and a dilation of 11.6 ± 5.3 % in 7 of 10 analyzed arterioles. The differences between all groups were not statistically significant.

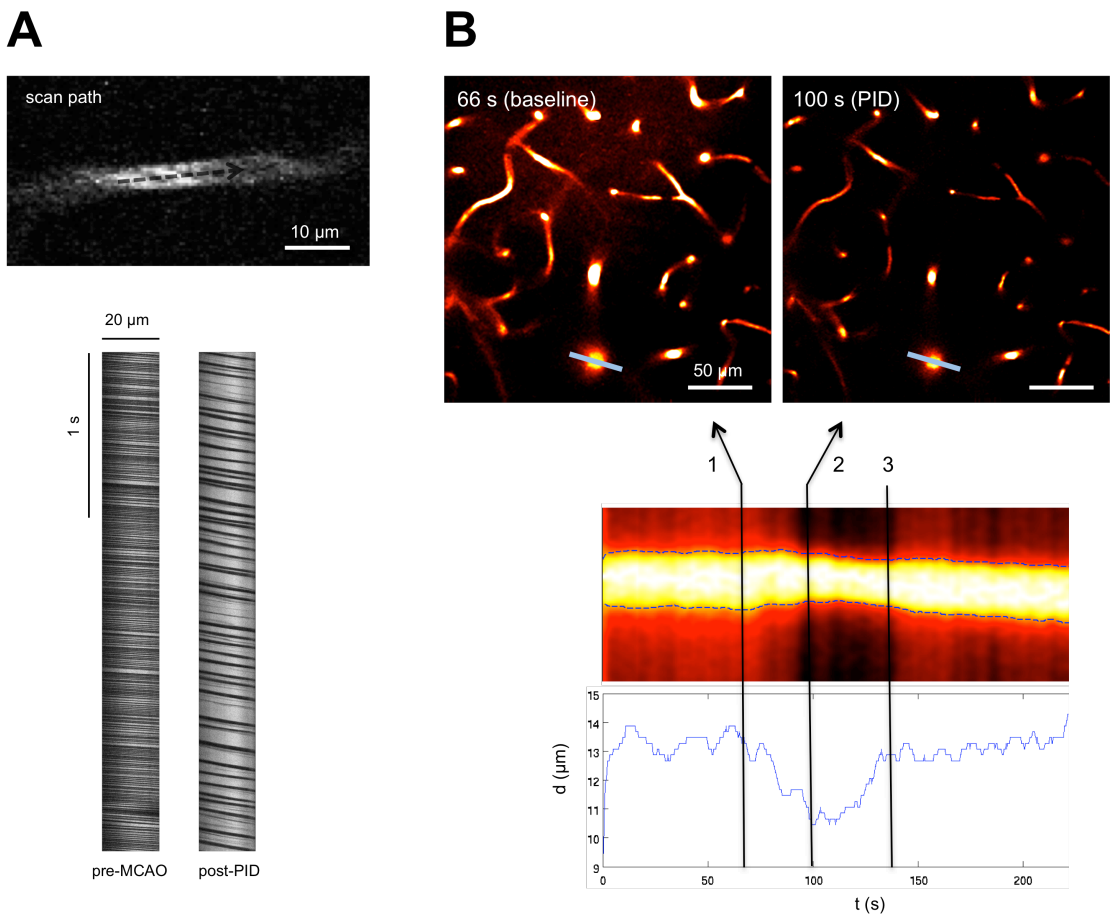

Figure 3-7: Cerebral blood flow measurement. A) Scan path of a line scan in a 2D image (top). Line scans along 20 µm following the scan path over 3 s before and after pMCAO (bottom). Shadows from erythrocytes are visible as black bands and serve for CBF measurement. B) Top: Snapshots from time-lapse series at baseline CBF (66 s) and reduced CBF during PID (100 s), the blue lines show the paths of diameter measurements. Bottom: Arteriolar diameter changes during PIDs were calculated with a MATLAB routine from the blue lines in the snapshots (top). The marked time points in the output document represent the artery diameters in the snapshots (top) at baseline diameter (1) and diameter during constriction (2). In this example, the diameter decreases from 13.5 to 10.5 µm due to arteriolar constriction during PID. Time point 3 shows the end point of constriction.

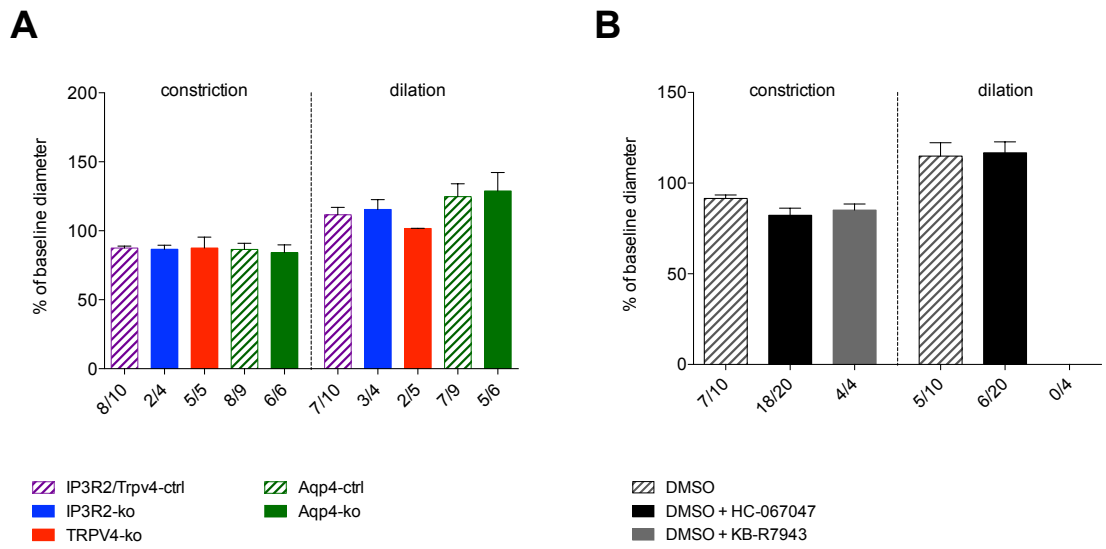

Figure 3-8: Diameter changes of penetrating arterioles during PID. Changes of arteriole diameter during PID in % of baseline diameter (before PID) show a reduction (constriction), followed by an increase (dilation). Individual numbers of constricting or dilating arterioles per analyzed arterioles are given on the x-axis. A) Diameter changes of IP3R2-kos, Trpv4-kos, and Aqp4-kos (filled bars) compared to their respective control groups (striped bars). B) Diameter change of wildtype animals after HC-067047, and KB-R7943 administration (filled bars) compared to controls after DMSO administration (striped bar). Data are represented as mean ± s.e.m.; $p>0.05$, Kruskal-Wallis test followed by Dunn's multiple comparisons test for comparison of 3 means or more, Mann-Whitney test for comparison of 2 means (Aqp4).

3.3.4 Imaging of Calcium Transients during the First Detected PID

It has previously been described that normoxic spreading depolarizations are accompanied by propagating calcium changes in astrocytes and neurons (Lauritzen et al., 2011).

Here, I found that similar changes also take place during PIDs. Propagating intracellular calcium transients in astrocytes and neurons were visible in the green spectrum as a wave traveling through the tissue (Figure 3-9 A). Signals from astrocytes and neurons were analyzed separately in defined ROIs placed over cell bodies. Examples of calcium increases in 4 different ROIs within astrocytes (A1 - A4) during a PID are shown in Figure 3-9 B. The direction of

the PID wave is reflected by the consecutive calcium increases in the marked cells.

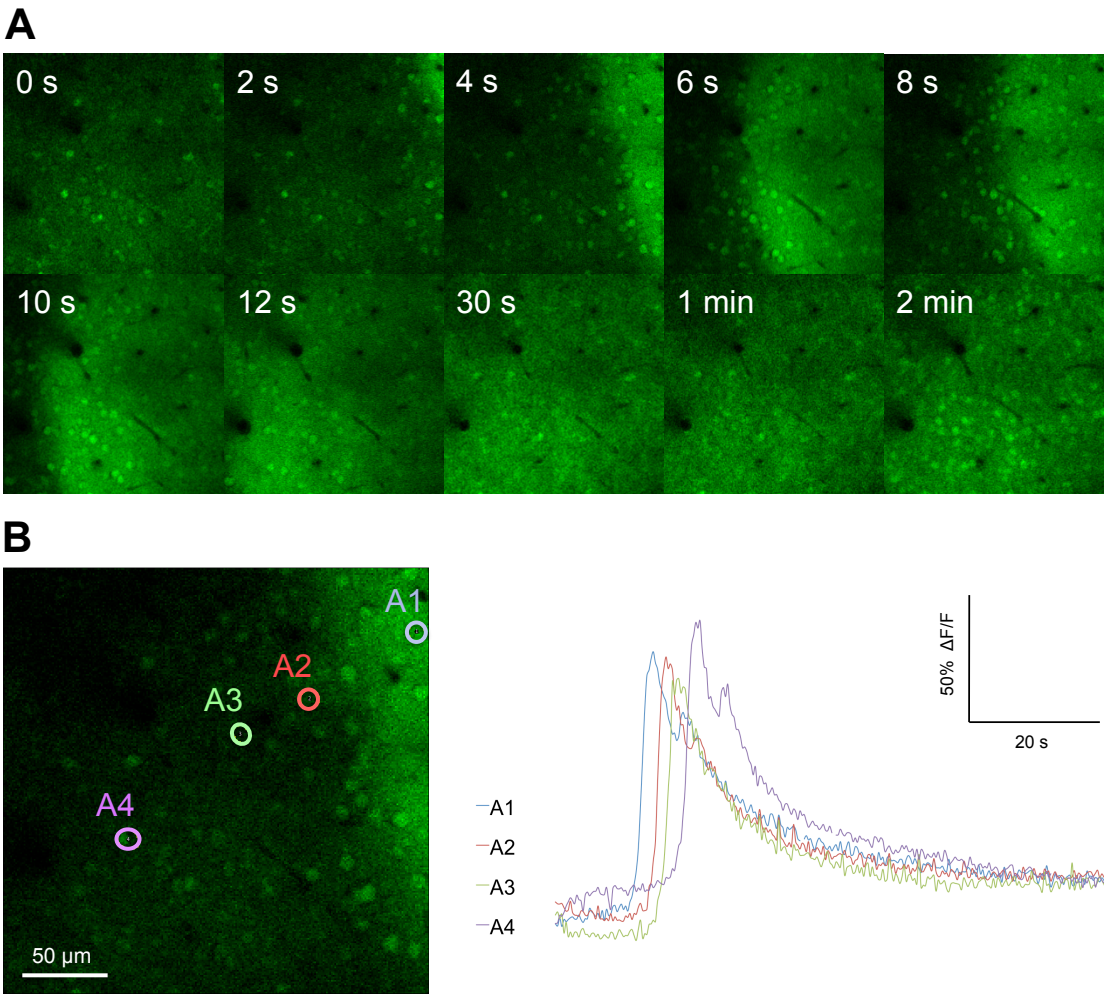

Figure 3-9: Rising calcium concentration in astrocytes during PID. A) A calcium wave is propagating from the right to the left side of the field of view. The signal of fluorescence intensity of OGB-1 AM was recorded in time-lapse series (3 Hz) through a 535/30 BP filter. B) On the left, colored circles in a snapshot from a time-lapse represent ROIs marking astrocytic somata. On the right, their normalized calcium transients are plotted in corresponding colors, demonstrating the chronology of calcium increases dependent on the wave direction.

Below, I will describe the statistical analysis of calcium changes in the different groups. Amplitude, FDHM, and time to peak of ΔF/F% were analyzed in each group for astrocytes and neurons. FDHM was only analyzed for ROIs that regained their half maximum ΔF/F% within the imaging time.

3.3.4.1 IP3R2 Deletion and Trpv4 Deletion Attenuated Calcium Signals during PIDs

Numbers of animals used for single cell calcium analysis are: n = 9 for IP3R2/Trpv4-ctrls, n = 5 for IP3R2-kos, n = 6 for Trpv4-kos, n = 7 for Aqp4-ctrls, and n = 6 for Aqp4-kos. Due to breeding problems of IP3R2- and Trpv4-knockout mice with Cx43-CFP$^{+/-}$ mice, astrocytes in two animals of the IP3R2 group and all of the Trpv4-kos were labeled with SR101, i. e. a fluorescent marker for astrocytes (Nimmerjahn et al., 2004). Because these mice did not have CFP expression, these mice were not used for edema measurements. In the following paragraphs, only statistically significant changes are described.

Astrocytic amplitude (A_A) and neuronal amplitude (A_N) of calcium signals in both IP3R2-kos (A_A = 41.5 ± 1.7 %, A_N = 62.0 ± 2.7 %, $p < 0.0001$) and Trpv4-kos (A_A = 45.1 ± 1.9 %, A_N = 56.5 ± 2.6 %, $p < 0.0001$) were drastically reduced compared to controls (A_A = 80.1 ± 2.1 %, A_N =108.3 ± 3.4 %), Figure 3-10 A, B.

Time to peak (TTP) of calcium signals was significantly increased in astrocytes and neurons of IP3R2-kos (TTP_A = 9.5 ± 0.6 s, $p < 0.0001$; TTP_N = 12.8 ± 1.4 s, $p = 0.0003$) compared to controls (TTP_A = 8.4 ± 0.5 s, TTP_N = 7.0 ± 0.4 s). In contrast, compared to the same controls, TTP was decreased in astrocytes and slightly increased in neurons of Trpv4-kos (TTP_A = 7.0 ± 0.1 s, $p = 0.0160$; TTP_N = 7.1 ± 0.2 s, $p < 0.0001$), Figure 3-10 E, F. A reduction of TTP was detectable in astrocytes of Aqp4-kos (TTP_A = 7.1 ± 0.4 s, $p = 0.0021$) compared to Aqp4-controls (TTP_A = 8.8 ± 0.5 s).

Full duration of half maximum (FDHM) of calcium signals was strongly increased in astrocytes of IP3R2-kos ($FDHM_A$ = 46.1 ± 6.2 s, $p = 0.0076$) and slightly increased in neurons of Trpv4-kos ($FDHM_N$ = 13.4 ± 0.6 s, $p = 0.0011$) compared to controls ($FDHM_A$ = 21.4 ± 1.6 s, $FDHM_N$ = 12.3 ± 0.8 s), Figure 3-10 C, D.

In summary, deletion of IP3R2 as well as of Trpv4 dampened the calcium signal in astrocytes and neurons (reduced amplitude). Deletion of Trpv4 accelerated the onset of the calcium signal in astrocytes (reduced TTP). In

contrast, deletion of IP3R2 extended the calcium signal (increased TTP, prolonged FDHM).

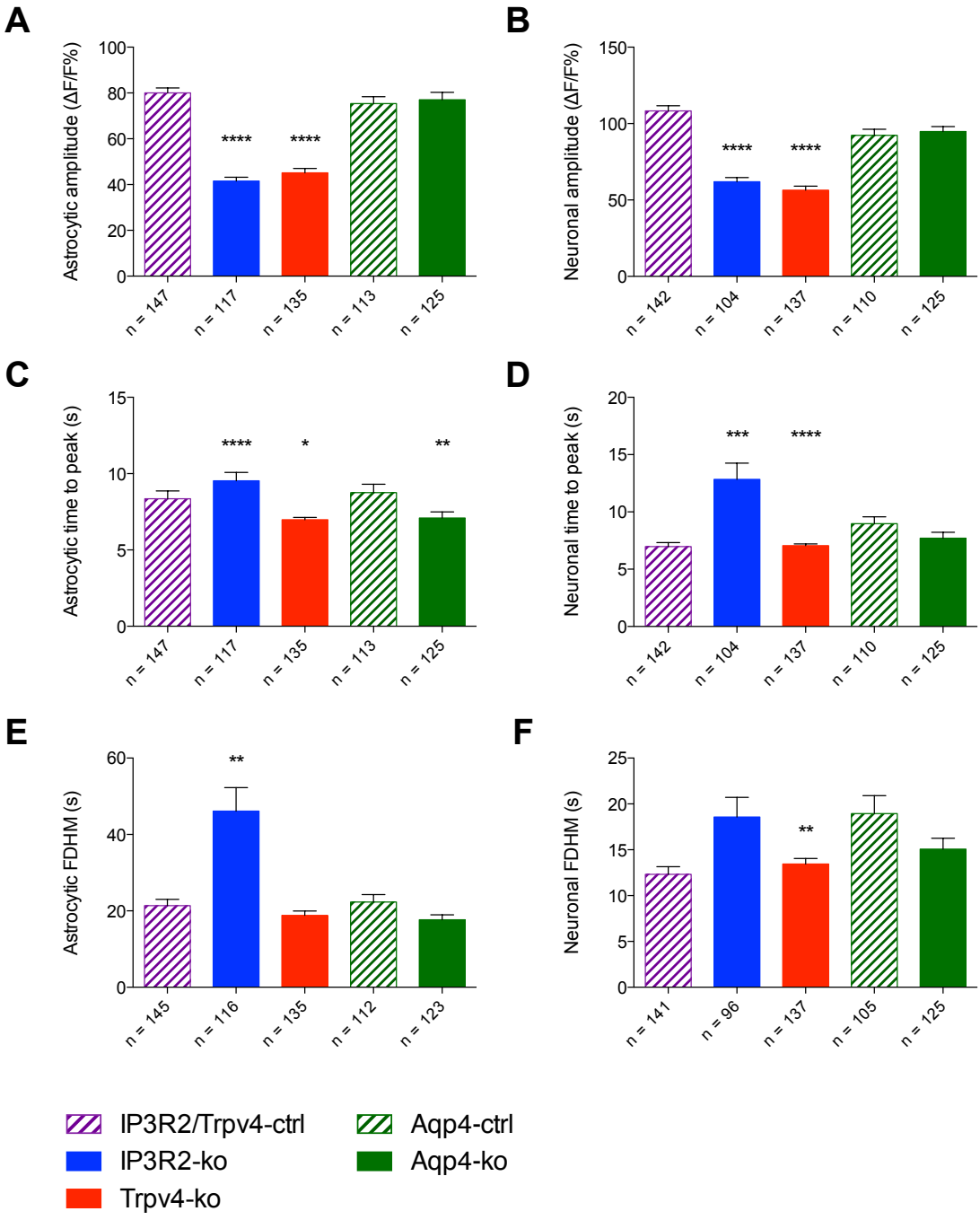

Figure 3-10: Analysis of calcium signals in astrocytes and neurons during PID in knockout mice. A) Astrocytic and B) neuronal amplitudes in IP3R2-kos and Trpv4-kos are reduced. C) Astrocytic and D) neuronal time to peak (TTP) are increased in IP3R2-kos and decreased in Trpv4-kos. Astrocytic TTP in Aqp4-kos is decreased. E) Astrocytic full duration of half maximum (FDHM) in IP3R2-kos and

F) neuronal FDHM in Trpv4-kos are increased. Numbers of analyzed cells are given below the bars, data are represented as mean ± s.e.m.; * p<0.05, ** p<0.01, *** p<0.001, **** p<0.0001, Kruskal–Wallis test followed by Dunn's multiple comparisons test for comparison of 3 means, Mann-Whitney test for comparison of 2 means (Aqp4).

3.3.4.2 Identification of DMSO as a Suitable Diluent for Calcium Imaging Experiments Using Pharmacological Inhibitors

As the blockers HC-067047 and KB-R7943 are only soluble in organic solvents, I tested the suitability of Cremophor and DMSO for calcium imaging. Numbers of animals used are: n = 9 for ctrls, n = 4 for Cremophor (1:10), and n = 3 for DMSO (1:1000). In the following results, only statistically significant changes are described.

The astrocytic and neuronal amplitude in the Cremophor group was strongly reduced (A_A = 45.0 ± 2.0 %, A_N = 63.1 ± 2.8 %, p < 0.0001), while the neuronal amplitude in the DMSO group was only slightly reduced (A_N = 91.5 ± 3.8 %, p = 0.0075) compared to wildtype controls (A_A = 80.1 ± 2.1 %, A_N = 108.3 ± 3.4 %), Figure 3-11 A, B.

TTP in astrocytes was reduced and increased in neurons in the Cremophor group (TTP_A = 8.2 ± 0.6 s, p = 0.0015; TTP_N = 8.0 ± 0.6 s, p = 0.0016) compared to controls (TTP_A = 8.4 ± 0.5 s, TTP_N = 7.0 ± 0.4 s), Figure 3-11 E, F.

FDHM of the astrocytic and neuronal calcium signal in the Cremophor group was strongly increased ($FDHM_A$ = 30.9 ± 2.2 s, $FDHM_N$ = 20.9 ± 1.5 s, p < 0.0001), while the neuronal signal in the DMSO group was slightly increased ($FDHM_N$ = 14.7 ± 1.5 s, p = 0.0069) compared to controls ($FDHM_A$ = 21.4 ± 4.9 s, $FDHM_N$ = 12.3 ± 0.8 s), Figure 3-11 C, D.

In summary, significant differences occurred under Cremophor that were stronger than when DMSO was used. Another advantage of DMSO is that it is diluted 100 x higher than Cremophor. Therefore, I selected DMSO as the diluent of pharmacological blockers for experiments that will be described in the subsequent paragraphs.

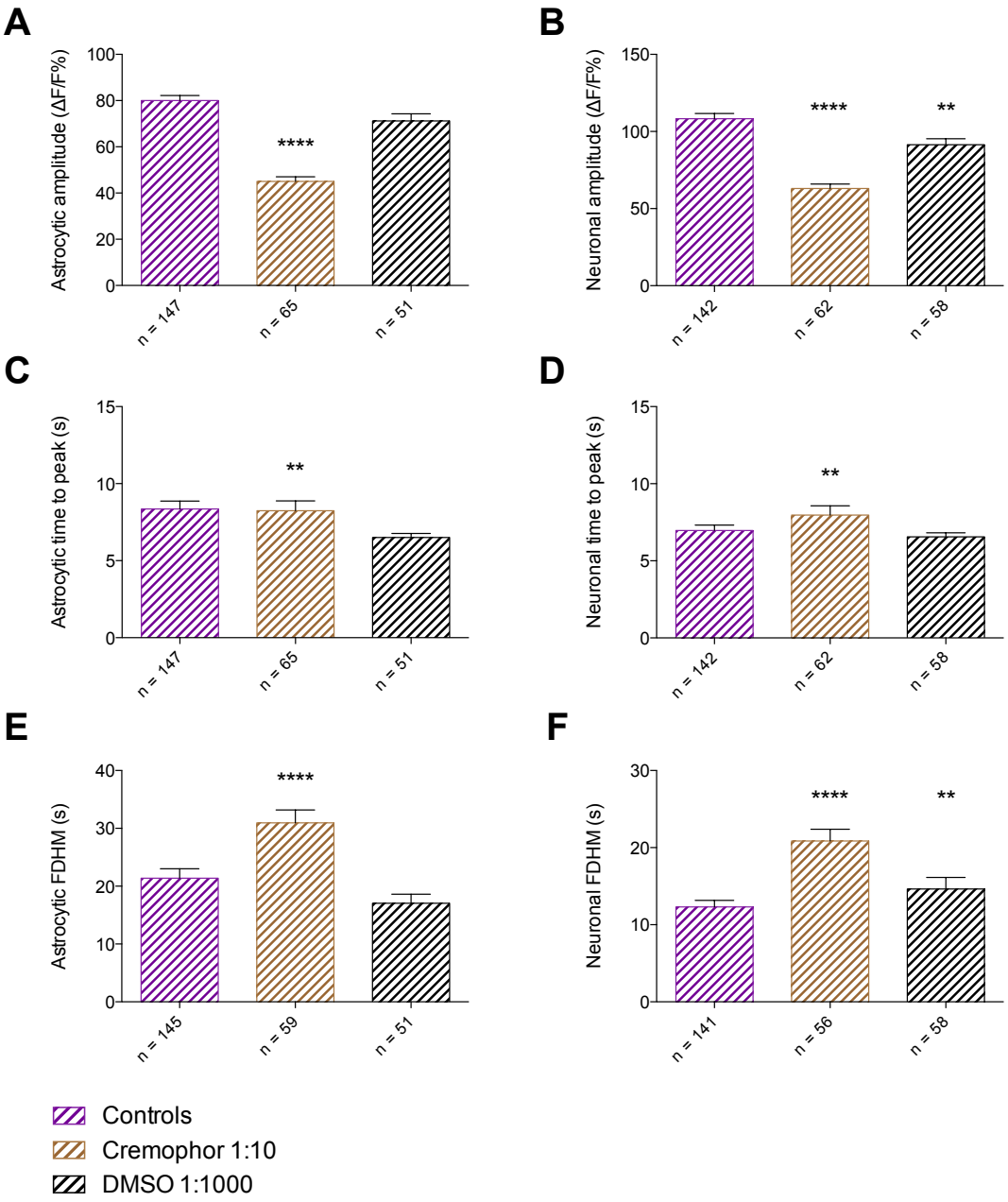

Figure 3-11: Cremophor influences calcium signals during PID stronger than DMSO. Cremophor and DMSO are tested as diluents for pharmacological blockers in 2-P calcium imaging experiments, compared to wildtype controls. In the Cremophor group, significantly lower astrocytic (A) and neuronal (B) amplitude, as well as lower astrocytic (C) and higher neuronal (D) TTP and higher astrocytic (E) and neuronal (F) FDHM were observed. DMSO data show considerably less pronounced changes (slightly lower amplitude and higher FDHM in neurons). Numbers of analyzed cells are given below the bars, data are represented as mean ± s.e.m.; ** $p<0.01$, **** $p<0.0001$, Kruskal–Wallis test followed by Dunn's multiple comparisons test.

3.3.4.3 TRPV4 Blockade Attenuated Calcium Signals in Astrocytes and Neurons, and NCX Blockade Slowed Neuronal Calcium Signals

In the next step, a TRPV4-blocker (HC-067047) and an NCX blocker (KB-R7943) were tested in separate groups against a control group (treated with DMSO). Numbers of animals used for calcium analysis under blocker application are: n = 3 for DMSO, n = 4 for DMSO + HC-067047, and n = 3 for DMSO + KB-R7943. In the following results, only significant changes are described.

HC-067047 reduced the amplitude in both astrocytes and neurons (A_A = 60.8 ± 4.0 %, p = 0.0041; A_N= 86.6 ± 5.4 %, p = 0.0057), while KB-R7943 reduced only the astrocytic amplitude (A_A = 59.2 ± 2.4 %, p = 0.0491) compared to DMSO controls (A_A = 71.2 ± 3.1 %, A_N = 91.5 ± 3.8 %), Figure 3-12 A, B.

Astrocytic and neuronal TTP was increased with HC-067047 (TTP_A = 7.4 ± 0.3 s, p = 0.0348; TTP_N = 7.5 ± 0.4 s, p = 0.0093) compared to DMSO controls (TTP_A = 6.5 ± 0.3 s, TTP_N = 6.5 ± 0.3 s). Compared to the same controls, neuronal TTP was strongly increased by KB-R7943 (TTP_N = 10.4 ± 1.1 s, p = 0.0049), Figure 3-12 E, F.

In summary, blockade of TRPV4 or NCX attenuated the calcium signal in astrocytes and neurons (reduced amplitude). Moreover, HC-067047 increased TTP in astrocytes and neurons, and KB-R7943 increased TTP in neurons.

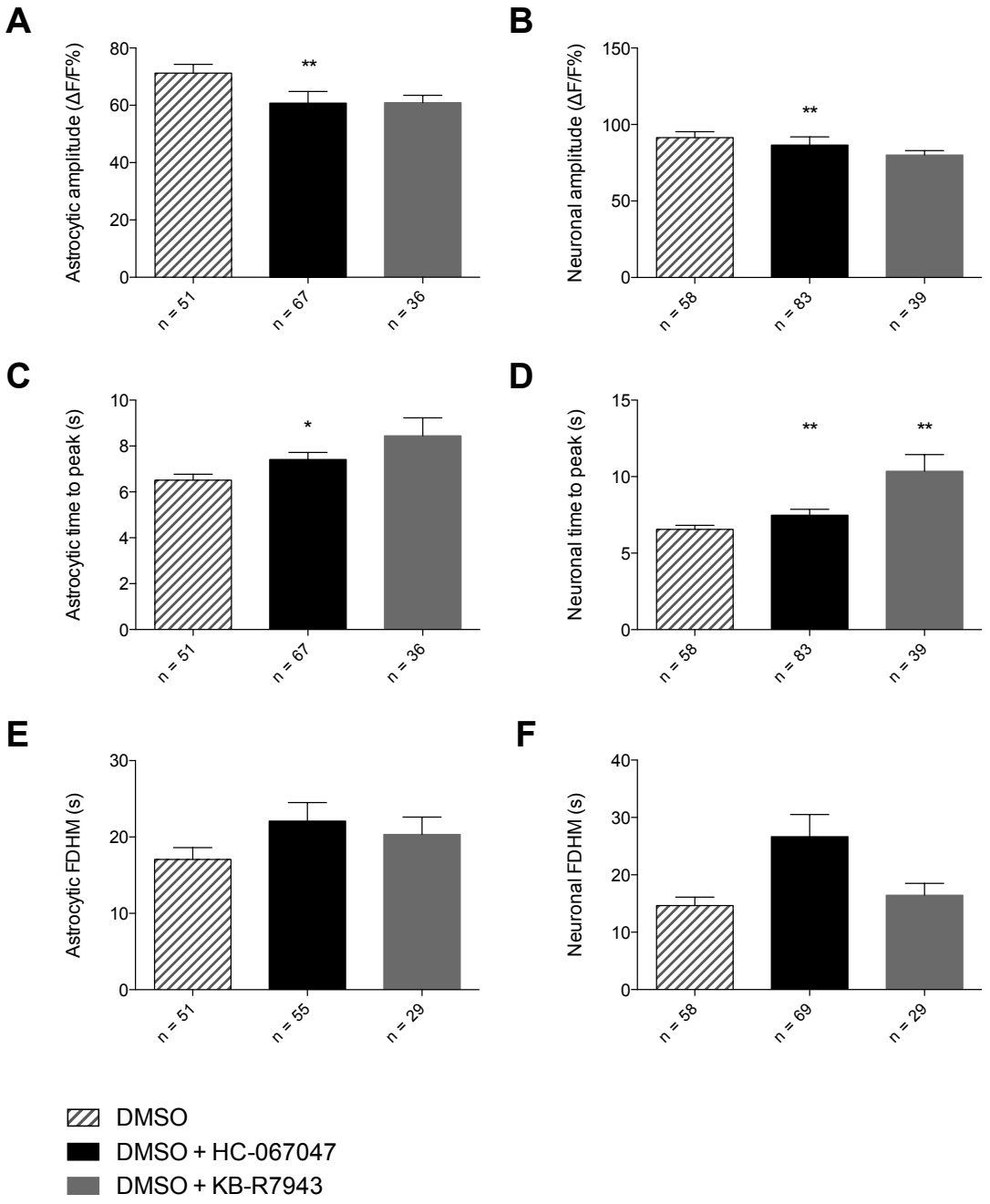

Figure 3-12: Analysis of calcium signals in astrocytes and neurons during PID after blocker application. Blockade of TRPV4 with HC-067047 shows a significant reduction of astrocytic (A) and neuronal (B) amplitude. Astrocytic TTP (C) is significantly increased with HC-067047 and D) neuronal TTP increased with either HC-067047 or KB-R7943. None of the blockers have significant effect on astrocytic (E) or neuronal (F) FDHM. Numbers of analyzed cells are given below the bars, data are represented as mean ± s.e.m.; * $p<0.05$, ** $p<0.01$, Kruskal–Wallis test followed by Dunn's multiple comparisons test.

3.3.4.4 Velocity of Calcium Waves within Astrocytes, Neurons, and Neuropil during PIDs

I separately calculated the propagation velocity of calcium waves associated with PIDs in astrocytes, neurons, and neuropil for all groups, as summarized in Figure 3-13. Numbers of animals used for velocity analysis are: n = 7 for IP3R2/Trpv4-ctrls, n = 4 for IP3R2-kos, n = 6 for Trpv4-kos, n = 6 for Aqp4-ctrls, n = 6 for Aqp4-kos, n = 2 for DMSO, n = 4 for DMSO + HC-067047, and n = 2 for DMSO + KB-R7943.

In control groups, mean velocities were 1.8 ± 0.4 mm/min for astrocytic propagation, 1.5 ± 0.2 mm/min for neuronal propagation, and 1.7 ± 0.3 mm/min for propagation within neuropil.

In all knockout groups, mean velocities did not differ significantly from controls (Figure 3-13 A). Also, after application of HC-067047 or KB-R7943, the velocity did not significantly change compared to DMSO (Figure 3-13 B). However, precise velocity analysis of calcium waves during PIDs was limited by: 1) the small size of the imaging window limiting the spatial range of measurement (max. 300 µm), 2) occasional circular progressions of PIDs sometimes preventing a clear identification of the main direction of PID propagation, 3) PID measurements only in the XY plane, neglecting PID propagation in the Z direction. Together, these factors were likely responsible for the high variation of mean velocity in the data (Figure 3-13).

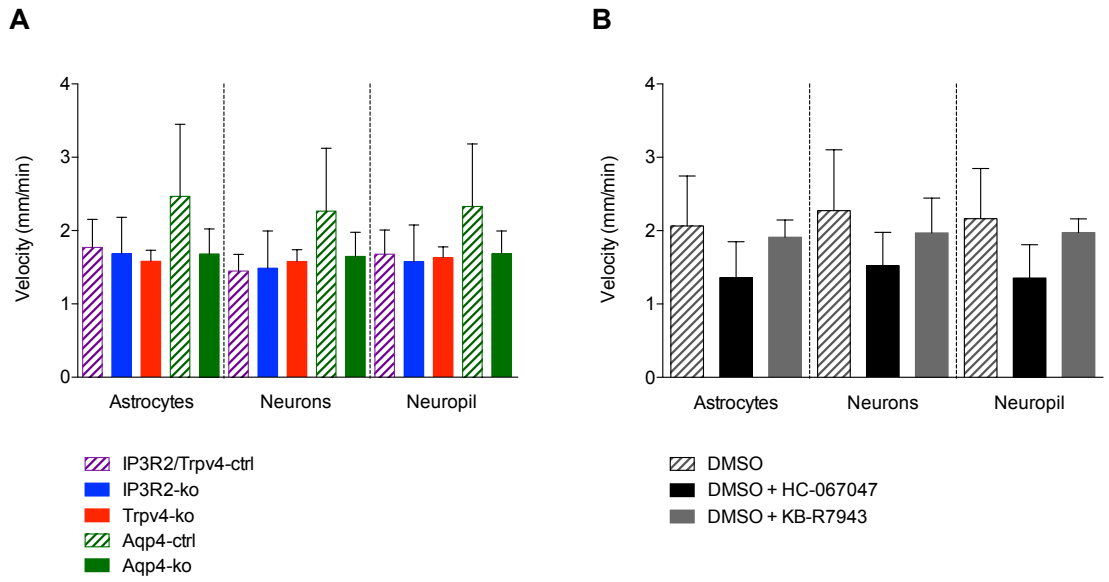

Figure 3-13: Velocities of calcium waves during PIDs in astrocytes, neurons, and neuropil. A) Velocities in IP3R2-kos, Trpv4-kos, and Aqp4-kos are not significantly different compared to according control groups. B) Velocities with HC-067047 or KB-R7943 also show no significant difference to DMSO. Data are represented as mean ± s.e.m.; $p>0.05$, Kruskal–Wallis test followed by Dunn's multiple comparisons test for comparison of 3 means, Mann-Whitney test for comparison of 2 means (Aqp4).

3.3.5 Edema Measurement

Because AQP4 has been described as a important mediator of cerebral edema under different pathophysiological conditions including stroke (Manley et al., 2000), I also measured astroglial edema development during PIDs in Cx43-CFPxAQP4-deficient mice compared to Cx43-CFP controls using a MATLAB cell tracking algorithm in Imaris (example shown in Figure 3-14 A).

Astrocyte edema was detectable after PID in 54.3 % of astrocytes in Aqp4-ctrls (107/197) and in 48.5 % of astrocytes in Aqp4-kos (80/165). Cell volumes before pMCAO and after the first PID are plotted in Figure 3-14 B: In both Aqp4-ctrls and Aqp4-kos, cell volume was significantly larger after PID, indicating astrocytic edema formation ($p < 0.0001$). Mean astroglial volume increase was 140.0 ± 9.0 μm^3 (32.0 ± 2.4 %) in Aqp4-ctrls, and 136.3 ± 10.5 μm^3 (33.5 ± 2.9 %) in Aqp4-kos. The differences between both groups were statistically not significant, indicating that AQP4 does not mediate acute astroglial edema during PIDs (Figure 3-14 C).

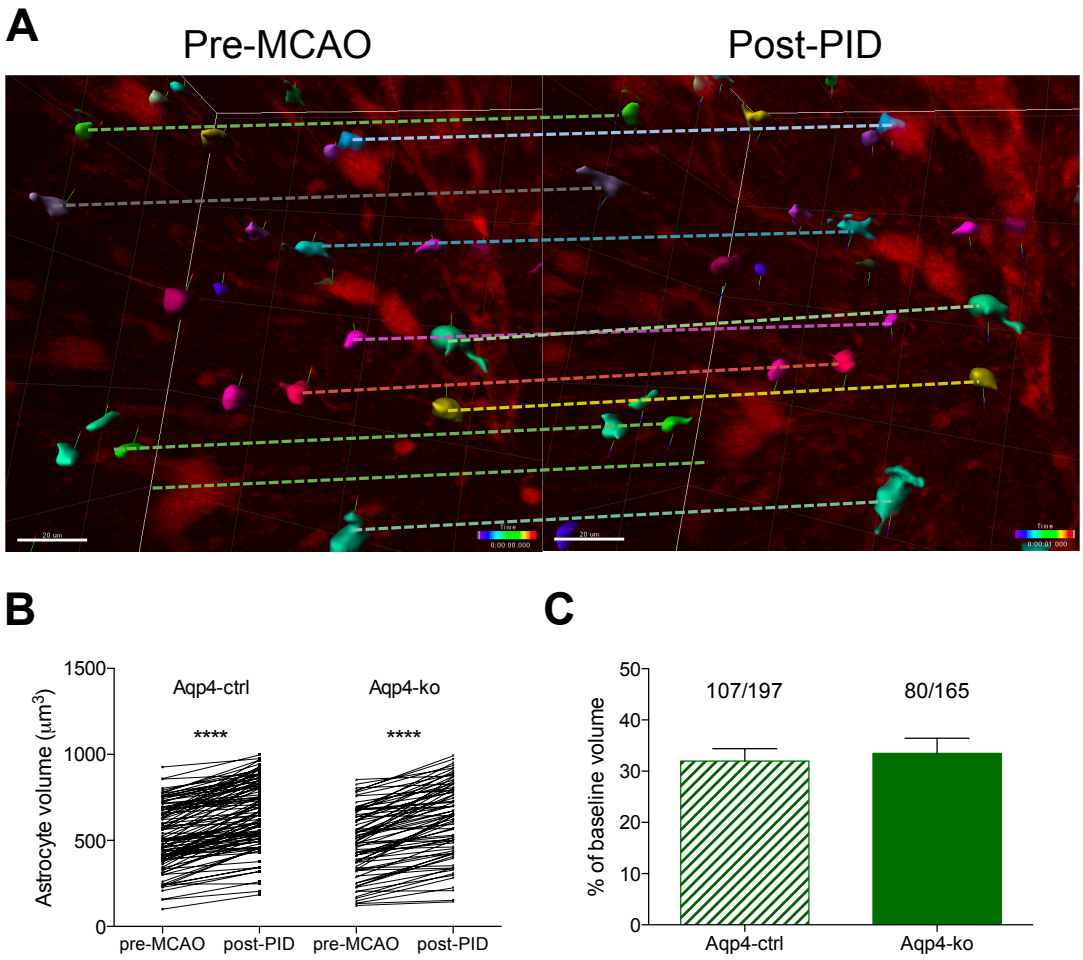

Figure 3-14: Cell size measurement with Imaris and edema estimation. A) Section of a 3D reconstruction of the CFP signal before MCAO and after detection of the first PID. Astrocytes within a 3D reconstruction were relocated by Imaris software by their CFP-Signal over 250 x 250 x 200 µm at the two different time points pre-MCAO and post-PID (Scale bar: 20 µm). Relocated identical cells are labeled in the same color, examples are connected by dashed lines. B) Cell sizes of astrocytes at pre-MCAO and post-PID show significant edema formation in both Aqp4-ctrl and Aqp4-ko. **** $p<0.0001$, paired t test after D'Agostino & Pearson omnibus normality test. C) Astrocyte edema formation in 107 of 197 astrocytes in Aqp4-ctrls and in 80 of 165 astrocytes in Aqp4-kos. Data are represented as mean ± s.e.m.; $p>0.05$, Mann Whiney test.

3.4 Systemic Physiological Monitoring

Pulse oximetry was carried out throughout experiments. The different knockout mouse lines showed no significant differences compared to controls. Mean oxygenation status of 97.8 ± 0.1 %, heart rate of 457.8 ± 12.2 min^{-1}, and breath

rate of 64.0 ± 4.1 min^{-1} were measured from mice at the end of experiments (n = 30, Appendix, Table 4).

3.5 Investigating PIDs Using a Genetic Calcium Indicator Approach – Preliminary Data

To overcome some of the limitations and constraints of pharmacological calcium indicators, and to enable long-term imaging experiments through chronic cranial windows in the future for the study of late PIDs or other phenomena, I intended to image PIDs with the endogenous calcium indicator GCaMP3, which can be conditionally expressed in specific cell types using the Cre/loxP system. Before 2-P imaging, I tested two astrocyte-specific Cre lines (Cx43-Cre and GLAST-Cre) for efficiency and specificity of Cre-mediated recombination after tamoxifen injection in the Ai38 mouse line.

3.5.1 Quantification

For the mouse lines Cx43-CreERT2:Ai38 (n = 2) and GLAST-CreERT2:Ai38 (n = 2), the amount of cortical GCaMP3 expression was quantified for comparison. Examples of coronal sections with immunofluorescent stainings that were used for quantification are shown in Figure 3-15 A. Under the Cx43 promoter, 15.95 ± 6.05 % of S100β-positive astrocytes expressed GCaMP3, while under the GLAST promoter, the amount was about 2-fold higher: 34.25 ± 2.35 % of S100β-positive cortical astrocytes expressed GCaMP3 (Figure 3-15 B). For analysis, only cells that were also positive for nuclear Hoechst stain signals were counted. Interestingly, cells of the GLAST-CreERT2:Ai38 line that have morphological characteristics of hippocampal neural progenitor cells also expressed GCaMP3 (Figure 3-15 C). However, in the cortex Cre recombination appeared to be specific for astrocytes in both lines.

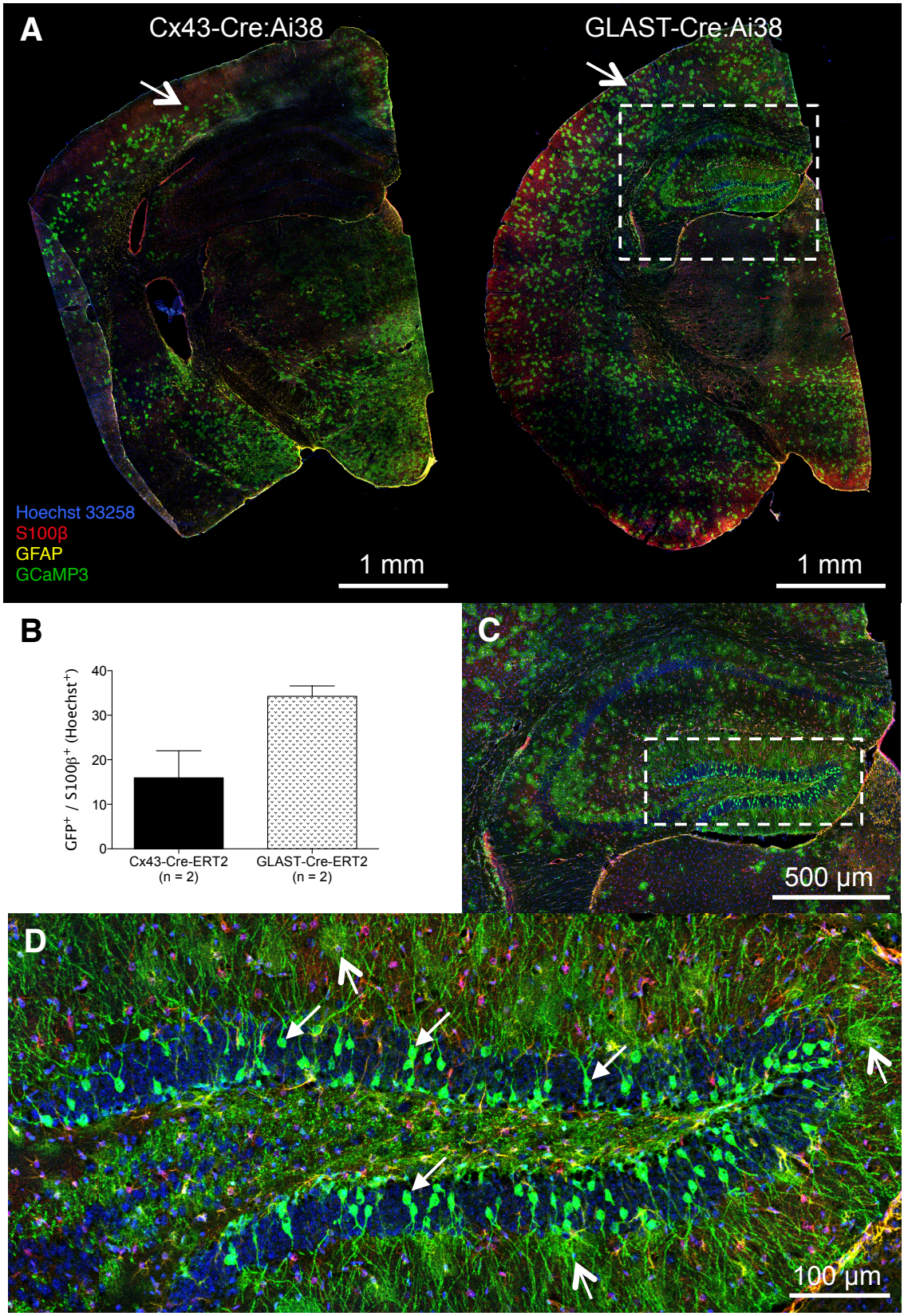

Figure 3-15: GCaMP3 expression in Cx43-CreERT2:Ai38 and GLAST-CreERT2:Ai38. A) Coronal cortical sections from the mouse lines Cx43-CreERT2:Ai38 (left) and GLAST-CreERT2:Ai38 (right) with nucleic stain (Hoechst 33258, blue) and immunolabelings: S100β (red) and GFAP (yellow) for

astrocytes, and GFP (green) for GCaMP3. Labeled cells in the cortex are identified as astrocytes (open arrows), both morphologically and by co-localization of S100β staining. B) Cortical GCaMP3 expression is quantified as the ratio of GFP positive cells to S100β positive cells, indicating greater efficiency of GLAST-CreERT2:Ai38. Data are represented as mean ± s.e.m.; $p>0.05$, Mann-Whitney test. C) Higher resolution of the boxed area in A indicates GCaMP3 expression in the hippocampus. D) Enlarged representation of the boxed area in C indicates GCaMP3 expression in astrocytes (open arrows) as well as in non-astrocytic cells (solid arrows) of the hippocampus in GLAST-CreERT2:Ai38 that show morphological characteristics of non-astrocytic cells, possibly representing neural progenitor cells.

3.5.2 Two-Photon Imaging of GLAST-CreERT2:Ai38 Mice

Because of its higher GCaMP3 expression rate, the GLAST-CreERT2:Ai38 mouse line was used for preliminary experiments using 2-P microscopy. In 3 of 6 transgenic animals, astrocytic calcium waves compatible with PIDs could be detected based on GCaMP3 fluorescence changes after pMCAO induction. Comparing the GCaMP3 signal to the artificial calcium indicator OGB-1, the signal primarily derived from astrocytic branches rather than from astrocytic somata (Figure 3-16 A compared to Figure 3-9 A). In Figure 3-16 B, ΔF/F% of the GCaMP3 calcium signals during the first PID are compared to ΔF/F% from measurements with OGB-1. The amplitude of ΔF/F with GCaMP3 was 83.6 % lower than with OGB-1 (13.1 ± 1.1 % vs. 80.0 ± 2.1 %, $p < 0.0001$), while TTP was reduced by 36.9 % (5.3 ± 0.1 s vs. 8.4 ± 0.5 s, $p = 0.0021$) and ΔF/F% returned to baseline nearly 2-fold faster, visible in a decreased FDHM by 46.4 % (11.7 ± 0.5 s vs. 21.4 ± 1.6 s, $p = 0.0137$).

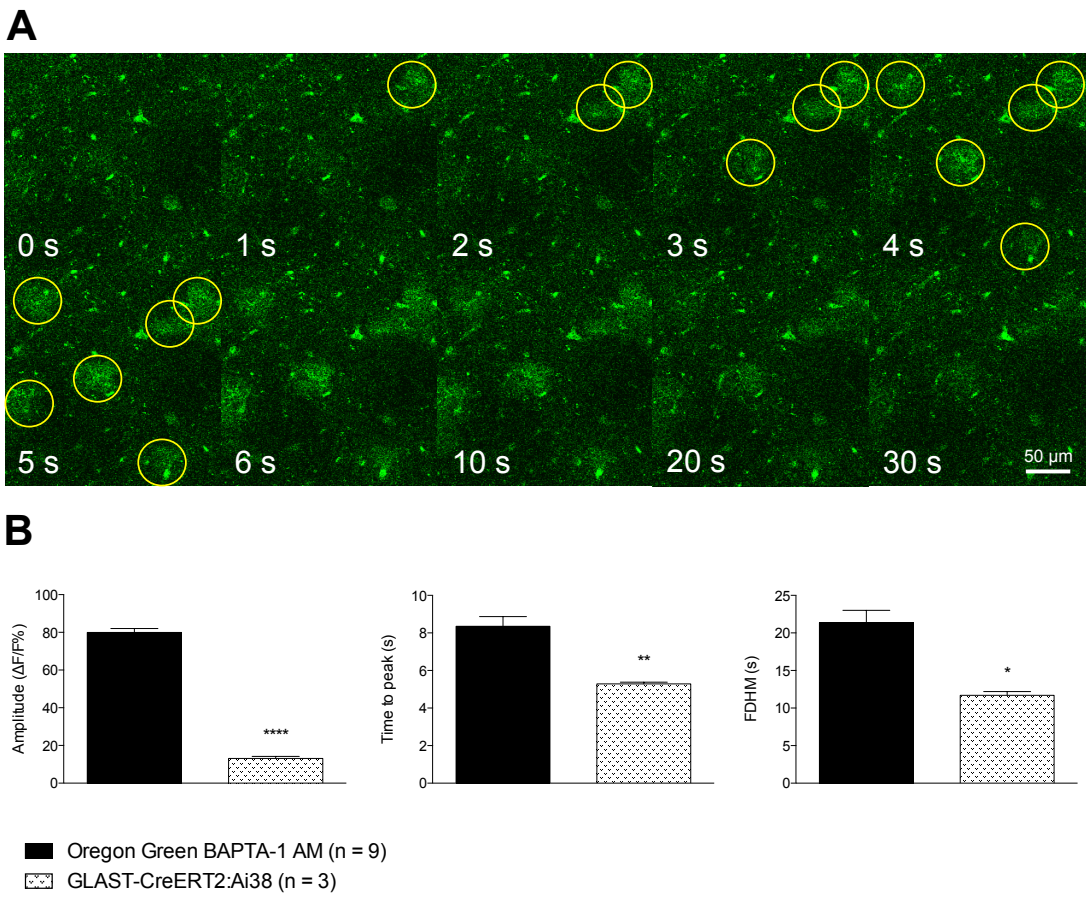

Figure 3-16: PID induced GCaMP3 calcium signals in GLAST-CreERT2:Ai38 mice. A) A calcium wave during a PID is predominantly visible in the branches of astrocytes, here propagating from the top right and heading to the bottom left of the imaging field. Astrocytes consecutively reached their maximum amplitude within 5 seconds (yellow circles). Within 30 s of PID, the calcium signal approached baseline levels. The signal of fluorescence intensity of GCaMP3 was recorded in time-lapse series (3 Hz) through a 535/30 BP filter. B) PIDs evoked calcium signals with smaller amplitude with GCaMP3 compared to OGB-1 AM, and TTP and FDHM of GCaMP3 signals were reduced compared to OGB-1 AM. Data are represented as mean ± s.e.m.; * $p<0.05$, ** $p<0.01$, **** $p<0.0001$, Mann-Whitney test.

4 Discussion

The main findings of this study are:

- Peri-infarct depolarizations in the cortical penumbra during acute focal ischemia are characterized by propagating calcium events in astrocytes and neurons that are accompanied by characteristic changes of local CBF and astroglial edema.
- Astroglial IP3R2 receptors, TRPV4 channels, and NCX transporters are important contributors to calcium elevations in astrocytes during PIDs.
- IP3R2 delay the onset of PIDs and reduce PID frequency, indicating that they may represent a novel target for stroke therapy.
- Astrocytic AQP4 channels do not mediate astroglial edema and calcium influx during PIDs.

4.1 *In vivo* Imaging of Early PIDs in the Cortical Penumbra after pMCAO

The penumbra is a brain region of intense interest in current stroke research, because CBF, albeit substantially reduced, is still sufficient to give cells the possibility to survive (Hossmann, 1996). However, the chance of survival for these cells will decline with time as cellular stress will progressively turn the penumbra into infarct core. PIDs have been linked to this conversion of cells from penumbra to infarct core (Mies et al., 1993). Unfortunately, the mechanisms of PIDs have remained poorly understood; mostly because studies directly investigating the cellular changes during PIDs have been missing. In this study, I

have established a technique to combine the pMCAO stroke model with cortical 2-P imaging in anesthetized mice, and to record calcium signals, CBF changes, and edema formation simultaneously in the ischemic penumbra at high temporal and spatial resolution.

Previous techniques of PID analysis were mostly limited to electrophysiological or laser speckle measurements. Stroke models in mice that could be combined with *in vivo* calcium imaging were limited to photothrombosis or global hypoxia (Murphy et al., 2008; Ding et al., 2009), which are both suboptimal for analyzing the penumbra. A photothrombosis creates a permanent ischemia with a consistent lesion size underneath the cortical surface, but only a very small and variable penumbra (Wang et al., 2010). In addition, a layer of dead cells in upper layers complicates imaging of the penumbra in deeper cortical layers. Meanwhile, the global ischemia model is generally not suited for imaging the penumbra, since CBF reduces globally >90 % from baseline for only 6-8 min, and does not reflect the pathophysiology of focal embolic stroke (Murphy et al., 2008).

Normoxic spreading depolarizations and PID-like depolarizations are accompanied by an increase of the intracellular calcium concentration in neurons and astrocytes (Basarsky et al., 1998; Somjen, 2001; Murphy et al., 2008; Pietrobon and Moskowitz, 2014) as well as by a characteristic sequence of CBF changes (Shin et al., 2006). With 2-P microscopy, I could visualize these astrocytic and neuronal calcium transients using the pharmacological calcium indicator OGB-1 AM (Figure 3-9). In parallel, I estimated PID-related CBF changes based on changes of arteriolar diameters (Figure 3-8). CFP expression by astrocytes was used to identify astrocytes and measure astrocytic edema. The advantages of this transgenic labeling of astrocytes compared to pharmacological labeling with SR101 (Nimmerjahn and Helmchen, 2012) are that SR101 can enter neurons in some models of ischemia (Thompson et al., 2006) and may have consequences for neuronal excitability (Kang et al., 2010a). I finally verified calcium transients in astrocytes by conditionally inducing astrocytic GCaMP3 (Figure 3-16).

4.2 The Role of Glial Calcium Transients during PIDs

4.2.1 Calcium Transients during PIDs are Mediated by IP3R2, TRPV4, and NCX

Previous studies showed that hypoxia in brain slices induces calcium influx into astrocytes (Duffy and MacVicar, 1996; Basarsky et al., 1998; Somjen, 2001; Pietrobon and Moskowitz, 2014), but the question has remained which pathways are responsible for these calcium transients. For this reason, I investigated calcium signals during PIDs in anesthetized mice after pMCAO induction with help of 2-P microscopy, and confirmed that PIDs are accompanied by propagating waves of calcium peaks in neurons and astrocytes.

Using IP3R2-ko and Trpv4-ko lines, I could demonstrate that these temporary astrocytic and neuronal calcium peaks are mainly dependent on calcium flux through IP3R2 and TRPV4, as evidenced by significantly lower calcium amplitudes during PIDs in both lines. Moreover, the temporal kinetics were also altered in these lines, as evidenced by an altered time to peak (TTP) component of the signal in both lines. The increased TTP in IP3R2-kos might indicate that release of calcium from internal stores during PIDs is an important contributor to the early phase of calcium transients in astrocytes. In turn, the decreased TTP in Trpv4-kos might indicate that membrane-anchored calcium channels such as TRPV4 are mainly responsible for the later phase of the calcium signals and might be activated after an initial calcium increase through internal stores. Alternatively, these differences might be explained by the different localizations of IP3R2 and TRPV4. IP3R2 are mainly localized in the cell soma, while TRPV4 are mostly localized in distal astrocytic processes (Benfenati et al., 2007). Since I mostly focused on somatic calcium changes for technical reasons, a reduced calcium influx into astrocytic branches through TRPV4 might redistribute calcium dynamics and accelerate calcium transients in the soma, ultimately resulting in a decreased TTP. Future studies using genetic calcium indicators – such as the ones investigated here in preliminary experiments – will

be necessary to better delineate the contribution of peripheral vs. somatic calcium changes in astrocytes during PIDs.

Another finding was that a residual calcium influx exists in either knockout line, suggesting additional pathways of calcium influx during PID other than through IP3R2 or TRPV4. The blockade of NCX in reverse mode in Cx-43-CFP mice indicated that part of these residual calcium transients in PIDs could be attributed to reverse-functioning NCX. During PIDs, high amounts of glutamate are released into the synaptic cleft and taken up into astrocytes by glutamate transporters, which thereby co-transport a large amount of sodium (Danbolt, 2001), (Parpura and Verkhratsky, 2012). The resulting outward gradient of sodium turns NCX into "reverse" mode and drives the inward transport of calcium (Annunziato et al., 2004).

Other remaining calcium influx might furthermore be gated by calcium-gated calcium release channels/Ryanodine receptors (Verkhratsky et al., 2012), a signaling cascade of which not much is known about yet and that might be addressed in future studies.

4.2.2 IP3R2 Mediate the Threshold for PIDs

Another interesting finding of this study was that IP3R2-kos have an elevated threshold for PIDs. The possible underlying reason is still an open question that will be addressed in future experiments, but one possibility is that IP3R2-dependent glutamate release from astrocytes is responsible for the effect on PID threshold.

Glutamate can be derived from different sources, including astrocytes, where glutamate release is triggered by an increase of intracellular calcium (Petravicz et al., 2008). Therefore, during hypoxia, IP3R2-dependent glutamate release from astrocytes might facilitate PID induction by raising glutamate levels in the synaptic cleft to a critical threshold. Released glutamate activates NMDA receptors, which are important for PID development (Basarsky et al., 1998; Ohta et al., 2001; Bornstädt et al., 2015) and also induce neuronal calcium influx. Thus, reduced glutamate release from astrocytes in IP3R2-kos could also explain the reduction of neuronal calcium amplitudes in my 2-P experiments. To further

investigate these questions, I plan to study glutamate release during PIDs by 2-P imaging of fluorescent markers of glutamate release such as iGluSnFR (Marvin et al., 2013) in future experiments.

However, IP3-dependent glutamate release from astrocytes seems not to be the only factor for PID initiation, as PIDs still occurred in IP3R2-ko mice, indicating that mice have a possibility for calcium signaling other than through IP3R2 in order to modulate neuronal function (Srinivasan et al., 2015).

4.2.3 AQP4 is not Involved in PID-related Calcium Signaling or Edema Formation

I showed that AQP4 is neither responsible for PID-related calcium transients nor for edema formation. AQP4 is exclusively expressed in astrocytic endfeet (Zador et al., 2009), where it induces calcium transients by itself (Thrane et al., 2011) or acts together with TRPV4 as a complex (Benfenati et al., 2011). AQP4 was identified as an astrocytic water channel that contributes to edema formation after stroke, induced by disruption of orthogonal array particles consisting of by two different isoforms of AQP4 (Badaut et al., 2011). In my experiments, I could see no differences concerning calcium transients or astrocyte edema formation during PIDs. Possibly, edema formation during PIDs is gated by other channels, e.g. by PANX1, which is known to open during hypoxia (Xiong et al., 2014). Meanwhile, AQP4 might play a more important role in later edema formation during stroke.

4.2.4 CBF Changes during PIDs

Although an interplay of astrocytic calcium elevations and neurovascular coupling has been proposed before (Zonta et al., 2003; Mulligan and MacVicar, 2004; Petzold and Murthy, 2011), the CBF response to PID was not influenced in any of the tested groups. These findings indicate that factors other than astroglial calcium changes are involved in CBF regulation during PIDs and are in line with a recent study, which observed that neurovascular coupling is independent of IP3R2 activity (Bonder and McCarthy, 2014).

4.3 Pathophysiological Relevance

Despite many years of research, treatment options for ischemic stroke are still very limited. It is important to gain knowledge about mechanisms that predominate in the penumbra during early stroke. It is conceivable that a higher PID threshold in the IP3R2-ko group could be associated with a smaller infarct volume and better outcome after transient MCAO. In addition, my experiments show that neuronal calcium transients are reduced by IP3R2 or Trpv4 deletion as well, indicating that detrimental calcium overload and excitotoxicity of neurons could be reduced by these mechanisms independently from their actions on PIDs. In future experiments, I plan to test these hypotheses in a transient MCAO model with a survival time of 72 hours followed by infarct volumetry and behavioral assessment. If reducing IP3R2 or TRPV4 activity proves beneficial in these experiments, these astroglial proteins might be attractive targets for future pharmacological, translational, and possibly clinical studies.

5 Appendix

Table 3: Residual CBF at different time points after pMCAO induction. TOI 1 was measured directly, TOI 2 approx. 1 hour, and TOI 3 4 hours after pMCAO induction. Data from n = 4 animals represent mean ± s.e.m..

Residual CBF (% of baseline)	**TOI 1**	**TOI 2**	**TOI 3**
ROI 1	76,3 ± 11,3	49,2 ± 5,3	52,4 ± 16,7
ROI 2	71,9 ± 10,3	47,4 ± 6,2	40,3 ± 18,0
ROI 3	74,5 ± 4,5	48,4 ± 6,4	54,2 ± 8,2
ROI 4	65,8 ± 6,3	43,1 ± 6,3	49,5 ± 6,9
ROI 5	54,1 ± 8,8	36,8 ± 6,1	39,3 ± 6,8
ROI 6	45,4 ± 7,8	31,0 ± 4,5	33,2 ± 6,0
ROI 7	36,4 ± 7,6	25,9 ± 4,2	29,7 ± 6,7
ROI 8	32,9 ± 7,6	23,7 ± 4,4	27,0 ± 7,9
ROI 9	30,3 ± 8,2	21,8 ± 4,3	16,7 ± 14,1
ROI 10	30,7 ± 6,2	22,6 ± 4,4	25,1 ± 5,5

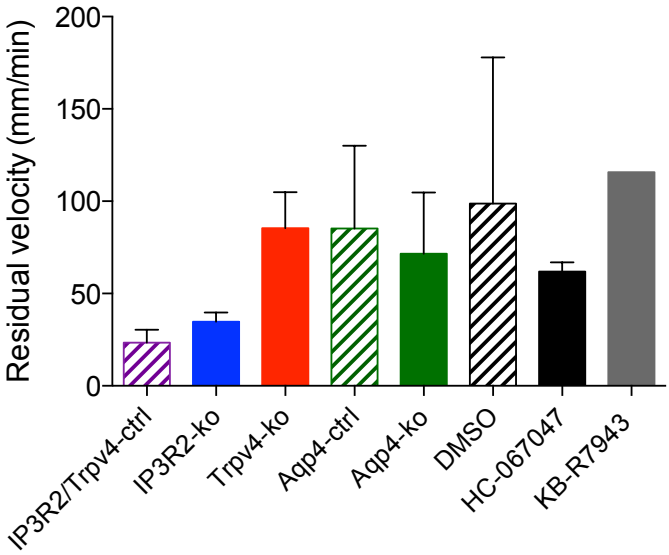

Figure 5-1: Residual velocity of erythrocytes after PID compared to pre-MCAO value measured from line scans taken during 2-P imaging. Animals are included from different experiments: IP3R2/Trpv4-ctrl: n = 5, IP3R2-ko: n = 2, Trpv4-ko: n = 2, Aqp4-ctrl: n = 4, Aqp4-ko: n = 5, DMSO: n = 2, DMSO + HC-067047: n = 2, DMSO + KB-R7943: n = 1. No significant differences were found between the groups. Data represent mean ± s.e.m., Kruskal–Wallis test followed by Dunn's multiple comparisons test for comparison of 3 means, Mann-Whitney test for comparison of 2 means (Aqp4). Mean residual velocity of 64.9 ± 12.4 mm/min is calculated (total: n = 23).

Table 4: Systemic physiological values after experiment. Blood oxygenation status, heart rate values, and breath rate values are presented for the different groups. Animals are included from different experiments: IP3R2/Trpv4-ctrl: n = 1, IP3R2-ko: n = 8, Trpv4-ko: n = 1, Aqp4-ctrl: n = 10, Aqp4-ko: n = 10. No significant differences were found between the groups. Data represent mean ± s.e.m.; $p>0.05$; Kruskal–Wallis test followed by Dunn's multiple comparisons test for comparison of 3 means, Mann-Whitney test for comparison of 2 means (Aqp4). Mean oxygenation status of 97.8 ± 0.1 %, mean heart rate of 457.8 ± 12.2 min^{-1}, and mean breath rate of 64.0 ± 4.1 min^{-1} are calculated (total: n = 30).

Systemic physiology	Blood oxygenation (SaO_2)	Heart rate (min^{-1})	Breath rate (min^{-1})
IP3R2/Trpv4-ctrl	97.8	430.0	66.0
Trpv4-ko	97.7 ± 0.3	471.6 ± 21.8	61.0 ± 7.1
IP3R2-ko	98.0	424.0	68.0
Aqp4-ctrl	97.7 ± 0.3	471.6 ± 22.8	70.2 ± 8.8
Aqp4-ko	98.0 ± 0.2	439.1 ± 23.0	57.6 ± 5.9

5.1 List of Figures

Figure 1-1: Ischemic stroke. 2
Figure 1-2: Expansion of severely hypoperfused cortex during AD and PIDs in acute focal ischemia (MCAO). 5
Figure 1-3: Putative cascade of damaging events in focal cerebral ischemia. 6
Figure 1-4: Astrocytic coupling in the neocortex compared to the corpus callosum. 8
Figure 1-5: Modulation of synaptic input within the tripartite synapse. 10
Figure 2-1: Schematic illustration of a mouse head from basal view during middle cerebral artery occlusion. 19
Figure 2-2: Schematic illustration of Oregon Green 488 BAPTA-1 AM (OGB-1) pressure injection. 21
Figure 2-3: Scheme of a mouse fixed in a stereotactic frame with an implanted cranial window. 22
Figure 2-4: Parameters used for PID analysis of DC potential measurement. 30
Figure 3-1: Laser speckle contrast imaging in different regions of the cranial window after pMCAO. A 33
Figure 3-2: DC shift in the penumbra and distant CBF change during a PID. 35
Figure 3-3: Analysis of detected PIDs in DC recordings. 37
Figure 3-4: Delay and reduction of PID incidences in IP3R2-kos versus controls after pMCAO induction. 38
Figure 3-5: Identification of a penetrating arteriole in the cortical vasculature. 39
Figure 3-6: Simultaneous *in vivo* 2-P imaging of CBF, calcium, and edema in Cx43-CFP$^{+/-}$ mice. 41
Figure 3-7: Cerebral blood flow measurement. 43
Figure 3-8: Diameter changes of penetrating arterioles during PID. 44
Figure 3-9: Rising calcium concentration in astrocytes during PID. 45
Figure 3-10: Analysis of calcium signals in astrocytes and neurons during PID in knockout mice. 47
Figure 3-11: Cremophor influences calcium signals during PID stronger than DMSO. 49
Figure 3-12: Analysis of calcium signals in astrocytes and neurons during PID after blocker application. 51
Figure 3-13: Velocities of calcium waves during PIDs in astrocytes, neurons, and neuropil. 53
Figure 3-14: Cell size measurement with Imaris and edema estimation. 54
Figure 3-15: GCaMP3 expression in Cx43-CreERT2:Ai38 and GLAST-CreERT2:Ai38. 56
Figure 3-16: PID induced GCaMP3 calcium signals in GLAST-CreERT2:Ai38 mice. 58
Figure 5-1: Residual velocity of erythrocytes after PID compared to pre-MCAO value measured from line scans taken during 2-P imaging. 66

5.2 List of Tables

Table 1: List of transgenic animals. 17
Table 2: List of primers. 26
Table 3: Residual CBF at different time points after pMCAO induction..... 65
Table 4: Systemic physiological values after experiment. 66

5.3 Abbreviations

2-P	2-Photon
A_A	Astrocytic amplitude
AD	Anoxic depolarization
A_N	Neuronal amplitude
AQP4	Aquaporin-4
BBB	Bood-brain barrier
CBF	Cerebral blood flow
CCA	Common carotid artery
CSD:	Cortical spreading depression
DAG	Diacylglycerol
DC	Direct current
ECA	External carotid artery
EEG	Electroencephalography
ER	Endoplasmic reticulum
$FDHM_A$	Astrocytic FDHM
$FDHM_N$	Neuronal FDHM
GECI	Genetically encoded calcium indicator
GqGPCR	Gq-G-protein coupled receptor
ICA	Internal carotid artery
IP3R2	Inositol triphosphate receptor 2
LDF	Laser Doppler flowmetry
NCX	Na^+/Ca^{2+} exchanger
NMDA	N-Methyl-D-aspartic acid
OAP	Orthogonal array particle
OGB-1	Oregon Green 488 BAPTA-1 AM
PANX1	Pannexin 1
PID:	Peri-infarct depolarization
PIP2	Phosphatidylinositol 4,5-bisphosphate
pMCAO	Permanent middle cerebral artery occlusion
ROI	Region of interest
ROS	Reactive oxygen species
RVD	Regulatory volume decrease
SCI	Spinal cord injury
SR101	Sulforhodamine 101
tMCAO	Transient middle cerebral artery occlusion
TOI	Time of interest
TRPV4	Transient receptor vanilloid 4
TTP_A	Astrocytic time to peak
TTP_N	Neuronal time to peak
TTX	Tetrodotoxin

6 List of Publications

Delekate A, Füchtemeier M, Schumacher T, Ulbrich C, Foddis M, Petzold GC (2014) Metabotropic P2Y1 receptor signalling mediates astrocytic hyperactivity in vivo in an Alzheimer's disease mouse model. Nat Commun 5:5422.

Ulbrich C, Zendedel A, Habib P, Kipp M, Beyer C, Dang J (2012) Long-term cerebral cortex protection and behavioral stabilization by gonadal steroid hormones after transient focal hypoxia. J Steroid Biochem Mol Biol 131:10–16.

7 Acknowledgement

Special thanks to Prof. Dr. Gabor Petzold for letting me work in his lab and submit my thesis today. He constantly contributed to my project with inventive ideas and open discussions. Thanks also for generously giving me the possibility to network on meetings with or without posters.

Thanks to Prof. Dr. Michael Pankratz from LIMES Institute of University of Bonn for the external supervision of my thesis.

Thanks to Dr. Martina Füchtemeier at Charité Berlin for my pleasant stay in her lab, where her technician Marco Foddis successfully improved my MCAO skills.

Thanks to Kevin Keppler and Dr. Hans Fried from Light Microscopy Facility for their advice and support at the microscopes.

Thanks to Dr. Christoph Möhl from the Image and Data Analysis Facility for writing various scripts and thereby making my analyses much faster, and to the IT staff for enabling this.

Thanks to Dr. Raman Saggu for her corrections on my thesis, Jan Peter and Armin Keller for genotyping my mice and their perpetual helpfulness in the lab, to Dr. Andrea Delekate, Dr. Toni Schumacher, Dr. Nicole Reichenbach, and Nancy El Deiry for always having an open ear and helpful advice, and to all the other colleagues not only for good teamwork in the lab, but also for amusing discussions in the Mensa, the kitchen and at the Spanier.

Thanks to all my awesome friends, who always give me the feeling of coming back after a week.

I thank my husband Fabian for being a great partner in all situations, for being patient with me, and for also commuting to work so we can wave at the Kölner Dom everyday.

Thanks to my big brothers Hanno and Bastian for watching me, and also to my parents a big thanks, without their trust and support over years I might not have reached this far!

8 Bibliography

Annunziato L, Pignataro G, Di Renzo GF (2004) Pharmacology of brain Na+/Ca2+ exchanger: from molecular biology to therapeutic perspectives. Pharmacol Rev 56:633–654.

Attwell D, Buchan AM, Charpak S, Lauritzen M, MacVicar BA, Newman EA (2010) Glial and neuronal control of brain blood flow. Nature 468:232–243.

Badaut J, Ashwal S, Obenaus A (2011) Aquaporins in cerebrovascular disease: a target for treatment of brain edema? Cerebrovasc Dis 31:521–531.

Basarsky TA, Duffy SN, Andrew RD, MacVicar BA (1998) Imaging spreading depression and associated intracellular calcium waves in brain slices. J Neurosci 18:7189–7199.

Benfenati V, Amiry-Moghaddam M, Caprini M, Mylonakou MN, Rapisarda C, Ottersen OP, Ferroni S (2007) Expression and functional characterization of transient receptor potential vanilloid-related channel 4 (TRPV4) in rat cortical astrocytes. Neuroscience 148:876–892.

Benfenati V, Caprini M, Dovizio M, Mylonakou MN, Ferroni S, Ottersen OP, Amiry-Moghaddam M (2011) An aquaporin-4/transient receptor potential vanilloid 4 (AQP4/TRPV4) complex is essential for cell-volume control in astrocytes. Proceedings of the National Academy of Sciences 108:2563–2568.

Bonder DE, McCarthy KD (2014) Astrocytic Gq-GPCR-linked IP3R-dependent Ca2+ signaling does not mediate neurovascular coupling in mouse visual cortex in vivo. Journal of Neuroscience 34:13139–13150.

Bornstädt von D, Houben T, Seidel JL, Zheng Y, Dilekoz E, Qin T, Sandow N, Kura S, Eikermann-Haerter K, Endres M, Boas DA, Moskowitz MA, Lo EH, Dreier JP, Woitzik J, Sakadzić S, Ayata C (2015) Supply-Demand Mismatch Transients in Susceptible Peri-infarct Hot Zones Explain the Origins of Spreading Injury Depolarizations. Neuron 85:1117–1131.

Butenko O, Dzamba D, Benesova J, Honsa P, Benfenati V, Rusnakova V, Ferroni S, Anderova M (2012) The increased activity of TRPV4 channel in the astrocytes of the adult rat hippocampus after cerebral hypoxia/ischemia. PLoS ONE 7:e39959.

Chuquet J, Hollender L, Nimchinsky EA (2007) High-resolution in vivo imaging of the neurovascular unit during spreading depression. Journal of Neuroscience 27:4036–

4044.

Danbolt NC (2001) Glutamate uptake. Progress in Neurobiology 65:1–105.

Day RE, Kitchen P, Owen DS, Bland C, Marshall L, Conner AC, Bill RM, Conner MT (2014) Human aquaporins: regulators of transcellular water flow. Biochim Biophys Acta 1840:1492–1506.

Degen J, Dublin P, Zhang J, Dobrowolski R, Jokwitz M, Karram K, Trotter J, Jabs R, Willecke K, Steinhäuser C, Theis M (2012) Dual reporter approaches for identification of Cre efficacy and astrocyte heterogeneity. FASEB J 26:4576–4583.

Desagher S, Glowinski J, Premont J (1996) Astrocytes protect neurons from hydrogen peroxide toxicity. J Neurosci 16:2553–2562.

Dijkhuizen RM, Beekwilder JP, van der Worp HB, Berkelbach van der Sprenkel JW, Tulleken KA, Nicolay K (1999) Correlation between tissue depolarizations and damage in focal ischemic rat brain. Brain Res 840:194–205.

Ding S, Wang T, Cui W, Haydon PG (2009) Photothrombosis ischemia stimulates a sustained astrocytic Ca2+ signaling in vivo. GLIA 57:767–776.

Dirnagl U, Iadecola C, Moskowitz MA (1999) Pathobiology of ischaemic stroke: an integrated view. Trends in Neurosciences 22:391–397.

Dirnagl U, Kaplan B, Jacewicz M, Pulsinelli W (1989) Continuous measurement of cerebral cortical blood flow by laser-Doppler flowmetry in a rat stroke model. J Cereb Blood Flow Metab 9:589–596.

Dong HW, The Allen Institute for Brain Science (2008) The Allen Reference Atlas, (Book + CD-ROM). Wiley.

Donnan GA, Baron J-C, Davis SM, Sharp FR (2007) The Ischemic Penumbra. CRC Press.

Dreier JP (2011) The role of spreading depression, spreading depolarization and spreading ischemia in neurological disease. Nat Med 17:439–447.

Duffy S, MacVicar BA (1996) In vitro ischemia promotes calcium influx and intracellular calcium release in hippocampal astrocytes. J Neurosci 16:71–81.

Dunn AK (2011) Laser Speckle Contrast Imaging of Cerebral Blood Flow. Ann Biomed Eng 40:367–377.

Dunn KM, Hill-Eubanks DC, Liedtke WB, Nelson MT (2013) TRPV4 channels stimulate Ca2+-induced Ca2+ release in astrocytic endfeet and amplify neurovascular coupling responses. Proceedings of the National Academy of Sciences 110:6157–6162.

Eckardt D, Theis M, Degen J, Ott T, van Rijen HVM, Kirchhoff S, Kim J-S, de Bakker JMT, Willecke K (2004) Functional role of connexin43 gap junction channels in adult mouse heart assessed by inducible gene deletion. Journal of Molecular and Cellular Cardiology 36:101–110.

Emsley JG, Macklis JD (2006) Astroglial heterogeneity closely reflects the neuronal-defined anatomy of the adult murine CNS. Neuron Glia Biol 2:175–186.

Giaume C, Koulakoff A, Roux L, Holcman D, Rouach N (2010) Astroglial networks: a step further in neuroglial and gliovascular interactions. :1–13.

Go AS et al. (2014) Heart disease and stroke statistics--2014 update: a report from the American Heart Association. Circulation 129:e28–e292.

Golgi C (1903) Opera omnia.

Haas B, Schipke CG, Peters O, Söhl G, Willecke K, Kettenmann H (2006) Activity-dependent ATP-waves in the mouse neocortex are independent from astrocytic calcium waves. Cereb Cortex 16:237–246.

Hankey GJ (2006) Potential new risk factors for ischemic stroke: what is their potential? Stroke 37:2181–2188.

Hartings JA, Rolli ML, Lu XCM, Tortella FC (2003) Delayed secondary phase of peri-infarct depolarizations after focal cerebral ischemia: relation to infarct growth and neuroprotection. Journal of Neuroscience 23:11602–11610.

Haustein MD, Kracun S, Lu X-H, Shih T, Jackson-Weaver O, Tong X, Xu J, Yang XW, O'Dell TJ, Marvin JS, Ellisman MH, Bushong EA, Looger LL, Khakh BS (2014) Conditions and Constraints for Astrocyte Calcium Signaling in the Hippocampal Mossy Fiber Pathway. Neuron 82:413–429.

Hayashi S, McMahon AP (2002) Efficient recombination in diverse tissues by a tamoxifen-inducible form of Cre: a tool for temporally regulated gene activation/inactivation in the mouse. Dev Biol 244:305–318.

Haydon PG (2001) GLIA: listening and talking to the synapse. Nat Rev Neurosci 2:185–193.

Henneberger C, Papouin T, Oliet SHR, Rusakov DA (2010) Long-term potentiation depends on release of D-serine from astrocytes. Nature 463:232–236.

Heuschmann P, Busse O, Wagner M, Endres M, Villringer A, Röther J, Kolominsky-Rabas P, Berger K (2010) Schlaganfallhäufigkeit und Versorgung von Schlaganfallpatienten in Deutschland. Akt Neurol 37:333–340.

Hossmann KA (1994a) Glutamate-mediated injury in focal cerebral ischemia: the excitotoxin hypothesis revised. Brain Pathol 4:23–36.

Hossmann KA (1994b) Viability thresholds and the penumbra of focal ischemia. Annals of Neurology 36:557–565.

Hossmann KA (1996) Periinfarct depolarizations. Cerebrovasc Brain Metab Rev 8:195–208.

Iadecola C, Nedergaard M (2007) Glial regulation of the cerebral microvasculature. Nat Neurosci 10:1369–1376.

Jeffs GJ, Meloni BP, Bakker AJ, Knuckey NW (2007) The role of the Na(+)/Ca(2+)

exchanger (NCX) in neurons following ischaemia. J Clin Neurosci 14:507–514.

Kang J, Kang N, Yu Y, Zhang J, Petersen N, Tian GF, Nedergaard M (2010a) Sulforhodamine 101 induces long-term potentiation of intrinsic excitability and synaptic efficacy in hippocampal CA1 pyramidal neurons. Neuroscience 169:1601–1609.

Kang SH, Fukaya M, Yang JK, Rothstein JD, Bergles DE (2010b) NG2+ CNS glial progenitors remain committed to the oligodendrocyte lineage in postnatal life and following neurodegeneration. Neuron 68:668–681.

Kettenmann H, Verkhratsky A (2013) Glial Cells. In, pp 475–506. New York, NY: Springer New York.

Kleinfeld D, Mitra PP, Helmchen F, Denk W (1998) Fluctuations and stimulus-induced changes in blood flow observed in individual capillaries in layers 2 through 4 of rat neocortex. Proc Natl Acad Sci USA 95:15741–15746.

Kofuji P, Newman EA (2004) Potassium buffering in the central nervous system. Neuroscience 129:1045–1056.

Kolominsky-Rabas PL, Heuschmann PU, Marschall D, Emmert M, Baltzer N, Neundörfer B, Schöffski O, Krobot KJ (2006) Lifetime cost of ischemic stroke in Germany: results and national projections from a population-based stroke registry: the Erlangen Stroke Project. Stroke 37:1179–1183.

Koulakoff A, Ezan P, Giaume C (2008) Neurons control the expression of connexin 30 and connexin 43 in mouse cortical astrocytes. GLIA 56:1299–1311.

Lauritzen M, Dreier JP, Fabricius M, Hartings JA, Graf R, Strong AJ (2011) Clinical relevance of cortical spreading depression in neurological disorders: migraine, malignant stroke, subarachnoid and intracranial hemorrhage, and traumatic brain injury. Journal of Cerebral Blood Flow & Metabolism 31:17–35.

Lenhossék von M (1891) Zur Kenntnis der Neuroglia des menschlichen Rückenmarkes.

Li X, Zima AV, Sheikh F, Blatter LA, Chen J (2005) Endothelin-1-induced arrhythmogenic Ca2+ signaling is abolished in atrial myocytes of inositol-1,4,5-trisphosphate(IP3)-receptor type 2-deficient mice. Circ Res 96:1274–1281.

Liedtke W, Friedman JM (2003) Abnormal osmotic regulation in trpv4-/- mice. Proc Natl Acad Sci USA 100:13698–13703.

Longa EZ, Weinstein PR, Carlson S, Cummins R (1989) Reversible middle cerebral artery occlusion without craniectomy in rats. Stroke 20:84–91.

Manley GT, Fujimura M, Ma T, Noshita N, Filiz F, Bollen AW, Chan P, Verkman AS (2000) Aquaporin-4 deletion in mice reduces brain edema after acute water intoxication and ischemic stroke. Nat Med 6:159–163.

Marvin JS, Borghuis BG, Tian L, Cichon J, Harnett MT, Akerboom J, Gordus A, Renninger SL, Chen T-W, Bargmann CI, Orger MB, Schreiter ER, Demb JB, Gan W-B, Hires SA, Looger LL (2013) An optimized fluorescent probe for visualizing

glutamate neurotransmission. Nat Meth 10:162–170.

Mies G, Iijima T, Hossmann KA (1993) Correlation between peri-infarct DC shifts and ischaemic neuronal damage in rat. Neuroreport 4:709–711.

Mori T, Tanaka K, Buffo A, Wurst W, Kühn R, Götz M (2006) Inducible gene deletion in astroglia and radial glia-A valuable tool for functional and lineage analysis. GLIA 54:21–34.

Moskowitz MA, Lo EH, Iadecola C (2010) The science of stroke: mechanisms in search of treatments. Neuron 67:181–198.

Mulligan SJ, MacVicar BA (2004) Calcium transients in astrocyte endfeet cause cerebrovascular constrictions. Nature 431:195–199.

Murphy TH, Li P, Betts K, Liu R (2008) Two-photon imaging of stroke onset in vivo reveals that NMDA-receptor independent ischemic depolarization is the major cause of rapid reversible damage to dendrites and spines. Journal of Neuroscience 28:1756–1772.

Nedergaard M, Rodríguez JJ, Verkhratsky A (2010) Glial calcium and diseases of the nervous system. Cell Calcium 47:140–149.

Nicotera P, Bellomo G, Orrenius S (1992) Calcium-mediated mechanisms in chemically induced cell death. Annu Rev Pharmacol Toxicol 32:449–470.

Nimmerjahn A, Kirchhoff F, Kerr JND, Helmchen F (2004) Sulforhodamine 101 as a specific marker of astroglia in the neocortex in vivo. Nat Meth 1:31–37.

Nizar K et al. (2013) In vivo stimulus-induced vasodilation occurs without IP3 receptor activation and may precede astrocytic calcium increase. Journal of Neuroscience 33:8411–8422.

Ohta K, Graf R, Rosner G, Heiss WD (2001) Calcium ion transients in peri-infarct depolarizations may deteriorate ion homeostasis and expand infarction in focal cerebral ischemia in cats. Stroke 32:535–543.

Parpura V, Verkhratsky A (2012) Homeostatic function of astrocytes: Ca(2+) and Na(+) signalling. Transl Neurosci 3:334–344.

Petravicz J, Fiacco TA, McCarthy KD (2008) Loss of IP3 receptor-dependent Ca2+ increases in hippocampal astrocytes does not affect baseline CA1 pyramidal neuron synaptic activity. Journal of Neuroscience 28:4967–4973.

Petzold GC, Murthy VN (2011) Role of Astrocytes in Neurovascular Coupling. Neuron 71:782–797.

Petzold GC, Windmüller O, Haack S, Major S, Buchheim K, Megow D, Gabriel S, Lehmann T-N, Drenckhahn C, Peters O, Meierkord H, Heinemann U, Dirnagl U, Dreier JP (2005) Increased extracellular K+ concentration reduces the efficacy of N-methyl-D-aspartate receptor antagonists to block spreading depression-like depolarizations and spreading ischemia. Stroke 36:1270–1277.

Pietrobon D, Moskowitz MA (2014) Chaos and commotion in the wake of cortical spreading depression and spreading depolarizations. Nature Publishing Group 15:379–393.

Roy CS, Sherrington CS (1890) On the Regulation of the Blood-supply of the Brain. The Journal of Physiology 11:85–158.17.

Schindelin J, Arganda-Carreras I, Frise E, Kaynig V, Longair M, Pietzsch T, Preibisch S, Rueden C, Saalfeld S, Schmid B, Tinevez J-Y, White DJ, Hartenstein V, Eliceiri K, Tomancak P, Cardona A (2012) Fiji: an open-source platform for biological-image analysis. Nat Meth 9:676–682.

Shen Z, Lu Z, Chhatbar PY, O'Herron P, Kara P (2012) An artery-specific fluorescent dye for studying neurovascular coupling. Nat Meth 9:273–276.

Shin HK, Dunn AK, Jones PB, Boas DA, Moskowitz MA, Ayata C (2006) Vasoconstrictive neurovascular coupling during focal ischemic depolarizations. J Cereb Blood Flow Metab 26:1018–1030.

Somjen GG (2001) Mechanisms of spreading depression and hypoxic spreading depression-like depolarization. Physiol Rev 81:1065–1096.

Srinivasan R, Huang BS, Venugopal S, Johnston AD, Chai H, Zeng H, Golshani P, Khakh BS (2015) Ca(2+) signaling in astrocytes from Ip3r2(-/-) mice in brain slices and during startle responses in vivo. Nat Neurosci 18:708–717.

Stosiek C, Garaschuk O, Holthoff K, Konnerth A (2003) In vivo two-photon calcium imaging of neuronal networks. Proc Natl Acad Sci USA 100:7319–7324.

Thompson RJ, Zhou N, MacVicar BA (2006) Ischemia opens neuronal gap junction hemichannels. Science 312:924–927.

Thrane AS, Rappold PM, Fujita T, Torres A, Bekar LK, Takano T, Peng W, Wang F, Rangroo Thrane V, Enger R, Haj-Yasein NN, Skare Ø, Holen T, Klungland A, Ottersen OP, Nedergaard M, Nagelhus EA (2011) Critical role of aquaporin-4 (AQP4) in astrocytic Ca2+ signaling events elicited by cerebral edema. Proceedings of the National Academy of Sciences 108:846–851.

Verkhratsky A (2006) Glial calcium signaling in physiology and pathophysiology. Acta Pharmacol Sin 27:773–780.

Verkhratsky A, Rodríguez JJ, Parpura V (2012) Calcium signalling in astroglia. Mol Cell Endocrinol 353:45–56.

Verkhratsky A, Steinhauser C (2000) Ion channels in glial cells. Brain Res Brain Res Rev 32:380–412.

Volterra A, Meldolesi J (2005) Astrocytes, from brain glue to communication elements: the revolution continues. Nat Rev Neurosci 6:626–640.

Vriens J, Watanabe H, Janssens A, Droogmans G, Voets T, Nilius B (2004) Cell swelling, heat, and chemical agonists use distinct pathways for the activation of the cation channel TRPV4. Proc Natl Acad Sci USA 101:396–401.

Wang T, Cui W, Xie Y, Zhang W, Ding S (2010) Controlling the Volume of the Focal Cerebral Ischemic Lesion through Photothrombosis. Am J Biomed Sci:33–42.

Xiong X-X, Gu L-J, Shen J, Kang X-H, Zheng Y-Y, Yue S-B, Zhu S-M (2014) Probenecid protects against transient focal cerebral ischemic injury by inhibiting HMGB1 release and attenuating AQP4 expression in mice. Neurochem Res 39:216–224.

Zador Z, Stiver S, Wang V, Manley GT (2009) Role of aquaporin-4 in cerebral edema and stroke. Handb Exp Pharmacol:159–170.

Zariwala HA, Borghuis BG, Hoogland TM, Madisen L, Tian L, De Zeeuw CI, Zeng H, Looger LL, Svoboda K, Chen T-W (2012) A Cre-dependent GCaMP3 reporter mouse for neuronal imaging in vivo. Journal of Neuroscience 32:3131–3141.

Zonta M, Angulo MC, Gobbo S, Rosengarten B, Hossmann K-A, Pozzan T, Carmignoto G (2003) Neuron-to-astrocyte signaling is central to the dynamic control of brain microcirculation. Nat Neurosci 6:43–50.

www.strokeassociation.org and www.edocamerica.com, 09/11/2014.